JGR Atmospheres

RESEARCH ARTICLE
10.1029/2025JD045812

Key Points:

- Under strong southwest monsoon, a low-level southeasterly component forms a wedge below the northwesterly component aloft in north Hainan Island
- Daytime mixing transports the northwesterly component downward, opposing southeasterly and creating convergence that initiates convection
- Sea breezes do not trigger the convection in north central Hainan Island while horizontal convective rolls play a minor role in this case

Correspondence to:
M. Xue,
mxue@ou.edu

Citation:
Wang, X., Xue, M., Zhu, K., Fan, Z., & Zhao, Z. (2026). Initiation of afternoon rainfall over north central Hainan Island, China: Important role of boundary-layer convergence produced by differential downward momentum transport by mixing in a typical case. *Journal of Geophysical Research: Atmospheres*, *131*, e2025JD045812. https://doi.org/10.1029/2025JD045812

Received 10 NOV 2025
Accepted 30 APR 2026

Author Contributions:
Conceptualization: Xiucheng Wang, Ming Xue
Data curation: Xiucheng Wang, Kefeng Zhu
Formal analysis: Xiucheng Wang
Funding acquisition: Ming Xue, Kefeng Zhu
Investigation: Xiucheng Wang
Methodology: Xiucheng Wang, Ming Xue, Ziqi Fan, Zhijun Zhao
Project administration: Ming Xue, Kefeng Zhu
Resources: Xiucheng Wang, Kefeng Zhu, Ziqi Fan, Zhijun Zhao
Software: Xiucheng Wang, Ziqi Fan, Zhijun Zhao
Supervision: Ming Xue, Kefeng Zhu
Validation: Xiucheng Wang, Ming Xue
Visualization: Xiucheng Wang, Ming Xue
Writing – original draft: Xiucheng Wang
Writing – review & editing: Xiucheng Wang, Ming Xue

Initiation of Afternoon Rainfall Over North Central Hainan Island, China: Important Role of Boundary-Layer Convergence Produced by Differential Downward Momentum Transport by Mixing in a Typical Case

Xiucheng Wang[1,2], Ming Xue[3], Kefeng Zhu[4,5], Ziqi Fan[6], and Zhijun Zhao[2]

[1]Key Laboratory of Mesoscale Severe Weather, Ministry of Education and School of Atmospheric Sciences, Nanjing University, Nanjing, China, [2]Meteorological Center, Northwest Air Traffic Management Bureau, Civil Aviation Administration of China, Xi'an, China, [3]Center for Analysis and Prediction of Storms and School of Meteorology, University of Oklahoma, Norman, OK, USA, [4]Nanjing Innovation Institute for Atmospheric Sciences, Chinese Academy of Meteorological Sciences–Jiangsu Meteorological Service, Nanjing, China, [5]Jiangsu Key Laboratory of Severe Storm Disaster Risk/Key Laboratory of Transportation Meteorology of CMA, Nanjing, China, [6]Shandong Meteorological Observatory, Jinan, China

Abstract During the summer monsoon season, with prevailing southwesterly winds, rainfall usually peaks in the afternoon on northern Hainan Island (HNI), China. On days of stronger prevailing winds, convection initiation (CI) often occurs in the north central HNI. Through simulations of a typical case of 20 June 2017 using a 2 km grid, we identify a primary CI mechanism over northern HNI that is driven by daytime boundary-layer (BL) vertical mixing and the resulting low-level convergence. Overnight and into the early morning, a wedge-like wind structure forms in the BL along an east-west vertical cross-section over northern HNI, which is characterized by a low-level southeasterly wind component, deeper in the east and shallower in the west, undercutting the northwesterly wind component aloft. By noon, surface-heating-induced BL vertical mixing transports the upper-level northwesterly component to the surface on the west side, creating a zone of convergence with the low-level southeasterly component from the east and triggering convection around noon. The wedge structure arises from the orographic effects of the mountains over southern HNI, when southerly flows bypassing the mountains from the west side gain more westerly component, while the flows climbing over the mountains descend on the leeside and cause isentropic surfaces to dip, lowering the layer possessing westerly component. Sensitivity experiments show that sea breezes are not responsible for initiating the convection in north central HNI, contrary to earlier suggestions, while BL horizontal convective rolls play only a secondary role in modulating the timing and locations of CI.

Plain Language Summary During the summer season when strong monsoon flows prevail over the Hainan Island of China, rainfall is usually the heaviest in the afternoon in the northern central part of the Island. Previous studies have suggested that the convergence forcing produced by inland-propagating sea-breeze fronts from the northeast and northwest coasts of the Island is responsible for producing the convection and precipitation, while boundary-layer convective roll circulations developing in the afternoon due to land surface heating also play a role. By analyzing numerical model simulations of a typical case in which precipitation occurred in the afternoon over north-central Hainan Island, we found that neither of the above two processes is responsible for initiating the precipitating convection. An alternative mechanism is proposed in which downward transport of westerly wind momentum to the surface in western-north Island creates a near-surface convergence zone with the easterly winds in eastern-north Island, and the convergence forces vertical lifting and convection. The mountains in southern Hainan Island are responsible for setting up the particular flow pattern and vertical structures that facilitate this mechanism. This mechanism is analogous to the convection initiation mechanism along drylines over slope terrains.

1. Introduction

Southern China, especially the coastal areas, is among the most vulnerable to heavy rainfall in China during the warm season (Zhang et al., 2017; Zheng et al., 2016). Heavy rain is typically associated with deep moist convection (DMC) and can result in significant losses and casualties in this highly developed and densely populated

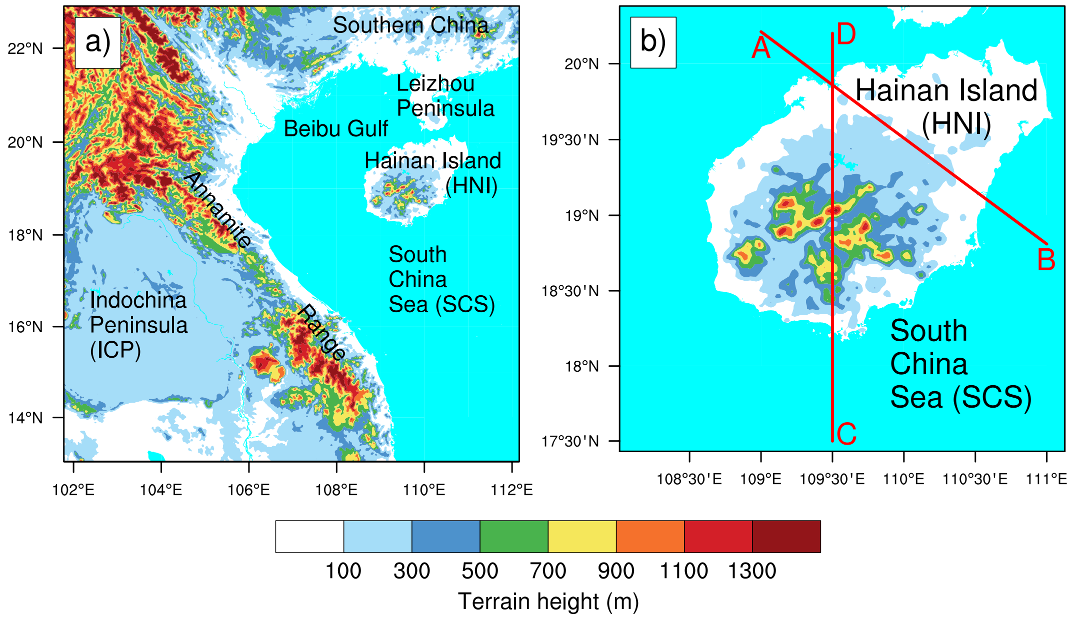

Figure 1. (a) Terrain height (shaded) of Hainan Island (HNI) and its vicinity, with Leizhou Peninsula, Beibu Gulf, Southern China, South China Sea (SCS), Indochina Peninsula (ICP), and Annamite Range marked. (b) A zoom-in figure of HNI with terrain height shaded. Lines A-B and C-D are for vertical cross sections later.

region. Due to the interactions among terrain, coastlines, land-sea breezes, monsoonal flows, and mid-latitude synoptic weather systems, the initiation of DMC in this region is complex and has attracted considerable research attention. Various convection initiation (CI) mechanisms in southern China are summarized below.

Land-sea breeze fronts are among the most common triggers for DMCs in this region. This mechanism frequently works near the shorelines of, for example, the south coasts of the Pearl River Delta (Chen et al., 2015, 2016), the Leizhou Peninsula, and the northern Hainan Island (Bai et al., 2020; Li et al., 2019; Liang & Wang, 2017; Zhu et al., 2017). Low-level jets are another significant trigger where coastlines and mountains are present and can force unstable flows to their level of free convection (Chen et al., 2014, 2015; Du & Chen, 2019; Du et al., 2020, 2022; Li et al., 2019). Researchers also found that outflows of convectively generated cold pools can initiate and maintain mesoscale convective systems by lifting oceanic moist flows (Liu et al., 2018; Wang et al., 2014). Additionally, synoptic systems such as cold fronts, shear lines, and low-level vortices frequently prime the mesoscale environment for CIs and occasionally directly trigger DMC.

Hainan Island (HNI) (see Figure 1), located in the southern tip of mainland China, is likewise highly susceptible to DMCs during the East Asian summer monsoon season (Zhang et al., 2017; Zheng et al., 2016). HNI features mountains in the south, mostly 300–900 m above mean sea level (MSL), and a plain in the north, mostly lower than 300 m MSL, with the opposite coastlines that are up to 150 km apart. DMCs usually occur in the afternoon in northern HNI during the southwesterly monsoon season. Most researchers attribute the primary trigger of the afternoon convection to the convergence associated with the collision of oppositely propagating sea-breeze fronts, whose effects are more pronounced under weak synoptic winds (Liang & Wang, 2017; Zhu et al., 2017, 2020). However, Liang and Li (2024) recently suggested that the convergence center on the lee side of HNI is attributed to a pressure gradient force induced by a lee-side high temperature center created by the advection of heated air.

However, most researchers believe that sea-breeze fronts are the principal trigger for DMCs on the northern HNI. In particular, Liang and Wang (2017) find that synoptic low-level winds over the HNI are relatively weak during summer and consider this a prerequisite for strong sea-breeze front interactions in the northern HNI. This appears reasonable because, in HNI, sea-breeze circulations can fully develop along the north coastlines and penetrate deep inland under weak offshore winds (generally below 2 m s^{-1}); when the southwesterly monsoon flows are strong, the sea-breeze flows tend to be swept offshore (Crosman & Horel, 2010). However, Du et al. (2022) demonstrate that two marine boundary-layer (BL) jets frequently appear to the west and east of the HNI during the summer, particularly in June. This suggests that winds over HNI are often relatively strong, especially in summer, contradicting previous findings. Furthermore, after studying the relationship of observed CI to ambient wind strength during April to June over the HNI, Zhu et al. (2021) found that the CI in the north is weak and is mainly located near the coastlines on low-wind days, but it strengthens and shifts inland on high-wind days (see their Figure 2). These findings do not support the sea-breeze triggering mechanism that works well only on weak synoptic wind days. As a result, the belief that sea-breeze fronts are the primary trigger for CI in northern HNI becomes questionable, at least on days of strong synoptic winds.

Zhu et al. (2021) attribute the enhancement and inland shift of convection over northern HNI on high wind days to horizontal convective rolls (HCRs) intersecting sea-breeze fronts (Atkins et al., 1995). However, this HCR mechanism fails to explain the inland shift of convection, since sea-breeze fronts are unlikely to penetrate deep inland under high-wind conditions (Crosman & Horel, 2010). Hence, our question is: Is there another mechanism responsible for the CI during the day over northern HNI, especially under high-wind conditions?

In our previous research (Wang et al., 2022), a rainfall case on 20 June 2017 was studied with a focus on the primary forcing mechanism of rainfall over southern HNI. We found that diurnal variations of southwesterly monsoon flows near the south coast of HNI are closely related to the downstream propagation of ageostrophic wind perturbations that developed over the upstream Indochina Peninsula (ICP) due to BL inertial oscillations (Blackadar, 1957); the arrival of peak positive onshore wind perturbations in the later morning at the southern HNI coast explains the precipitation peak at that time and location. In that case, the daily mean 950 hPa southwesterly winds reached 8–10 m s^{-1} in southern HNI and 6–8 m s^{-1} in northern HNI. Low-level jets appeared to the west and east of HNI with core speeds of over 12 m s^{-1}. Generally, with such strong winds, inland propagation of sea-breeze fronts on the lee side would stall near the coastlines (Crosman & Horel, 2010). However, rainfall in northern HNI first starts inland of northern HNI around noon, and heavy rain ensues. Therefore, sea-breeze fronts do not appear to be responsible for the inland CI in that case.

In this paper, we focus on investigating the forcing mechanism of CI in northern HNI on 20 June 2017. After carefully examining the roles of various processes, such as sea-breeze fronts, BL vertical mixing, HCRs, and terrains within numerical simulations, we find a CI mechanism at work on that day that had not been discussed before in the same context. The mechanism works due to the enhancement of near-surface wind convergence when stronger westerly winds in the upper BL and above on the west side of the HNI are brought down to the surface by daytime BL vertical mixing. The surface wind on the eastern part of HNI remains easterly in a representative east-west cross section, with an initially deeper layer of easterly flows that exhibit a wedge shape. The convergence zone occurs on the inland plain of northern HNI and works more effectively on days with stronger southwesterly monsoon winds that produce specific flow patterns on the leeside of southern HNI mountains. In contrast, sea-breeze fronts or HCRs do not play a primary role in the CI.

The paper is organized as follows. Section 2 presents the methodology and data used in this study. Section 3 compares the observed and simulated CI and rainfall, while Section 4 discusses the primary CI mechanisms based on detailed analyses of various processes in control and sensitivity experiments. Section 5 gives a summary and conclusions.

2. Methodology and Data

Convection-permitting simulations with the Weather Research and Forecasting Model (WRF-ARW v3.9.1.1; Skamarock et al., 2008) were performed from 0800 LST 19 June to 0800 LST 21 June 2017 to reveal the mechanism of inland CI on northern HNI in this case. The simulation in our prior paper (Wang et al., 2022) is used as the control simulation (CTRL run hereafter) in the present paper, whose initial and lateral boundary conditions are based on the National Centers for Environmental Prediction (NCEP) six-hourly Final (FNL) Operational Global Analysis data. The model setup of the CTRL run includes a 2 km horizontal grid spacing, 35 vertical levels, and one domain with 601×601 grid points, centered at the point (19°N, 108°E), west of the HNI. The domain is large enough to cover ICP upstream of HNI so that physical processes over ICP and their influences on HNI can be included. Main physics options used in our simulations contain the Yonsei University (YSU) planetary BL (PBL) scheme (Hong et al., 2006), the Thompson microphysics scheme (Thompson et al., 2008), the Rapid Radiative Transfer Model for Global Climate Models (RRTMG) longwave and shortwave radiation schemes (Iacono et al., 2008), the unified Noah land surface model (Livneh et al., 2011), and the revised MM5 Monin–Obukhov surface-layer scheme (Jiménez et al., 2012).

To quantify momentum changes due to PBL vertical mixing, two new diagnostic variables—RUBLTEN_ACC and RVBLTEN_ACC—were added to the YSU PBL scheme code. They represent the accumulated changes to the zonal (u) and meridional (v) wind components due to PBL mixing starting from the model initial time. Such changes are examined when we discuss the PBL mixing effect on near-surface convergence. In addition, the momentum eddy diffusivity coefficient K_m (EXCH_M in WRF), a good indicator of the vertical mixing strength, is output to aid the interpretation.

Three additional sensitivity experiments—namely FixTSK, NoRAIN, and NoTER—were performed to provide supplementary support to our proposed CI mechanism. FixTSK is identical to CTRL, except that the surface skin temperature (TSK) over HNI is fixed to its initial value at 0800 LST on 19 June. The NoRAIN experiment is identical to CTRL except that microphysical processes over HNI are suppressed within the Thompson scheme. In NoTER, the terrain height for HNI grid points is set to 0 m within the model.

FixTSK is designed to suppress land surface heating–related processes, including land–sea breezes associated with land–sea thermal contrast and BL vertical mixing driven by daytime surface heating. NoRAIN aims to reveal the role of BL HCRs in rainfall initiation by removing the feedback from precipitation. NoTER is conducted to examine the influence of the southern mountains of HNI on the circulations over and around HNI and the effect on rainfall initiation.

Aside from driving the simulations at the lateral boundaries, the NCEP global model final analysis (FNL) data with a grid resolution of 0.25° × 0.25° were also used to illustrate the synoptic background conditions. The merged rainfall data (Shen et al., 2014), with a grid spacing of 0.1° × 0.1°, which combine satellite-derived rainfall from the NCEP Climate Prediction Center MORPHing Technique (CMORPH) (Joyce et al., 2004) and China's hourly rain gauge observations, as well as hourly 10-m wind observations from automatic weather stations and the upper-air sounding at 0800 LST on 20 June 2017 from Haikou radiosonde station (station ID: 59758) on northern HNI, are employed to evaluate the simulations. Furthermore, a 10-year climatology (2010–2019) of 950-hPa winds and geopotential heights is constructed based on the 0.25° × 0.25° monthly mean pressure-level data from the fifth-generation ECMWF reanalysis (ERA5; Hersbach et al., 2023) to assess the representativeness of the flow patterns in the present case.

3. Observed and Simulated Rainfall Initiations on Northern HNI

Based on the FNL data at 0800 LST on 20 June 2017, the western Pacific subtropical high at 500 hPa is located over the Philippines, with southwesterly winds flowing over the ICP and the northern South China Sea (SCS). A low-pressure center sits over southern China at 850 hPa with a nearly north-south-oriented monsoonal trough along the ICP east coast (see Figure 2). At 950 hPa, strong southwesterlies (wind speed ≥10 m s^{-1}) originating from the ICP coasts blow across the Beibu Gulf and the strait upstream of HNI; the flow pattern resembles the ERA5 ten-year mean in June, except for the wind speed, that is, about 2 m s^{-1} stronger (see Figure 3). Overall, the low-level flow pattern on this day can, to a great extent, represent the climatology of June.

In observations, despite localized light rainfall briefly appearing in northern HNI before 1100 LST (Figure 4a), the main rainfall episode begins between 1100 LST and 1200 LST near 110°E (Figure 4b). It develops quickly afterward and peaks at 1500 LST (Figure 4c). The CTRL run reproduces rainfall initiation spatially and temporally reasonably well (cf. Figures 4e and 4b). Furthermore, the subsequent evolution of afternoon rainfall in CTRL is generally consistent with observations (cf. Figures 4f and 4c), albeit with certain spatial discrepancies in the rainfall distribution. Specifically, simulated rainfall extends farther offshore along the northern coast compared with observations, whereas along the eastern coast it spreads less offshore and remains closer to the shoreline. Despite these differences, the diurnal rainfall cycle over the island—both over the southern and northern regions—agrees well with the observations. Since the primary objective of this study is to understand the primary dynamic and thermodynamic forcing mechanisms for the initiation of convection and rainfall, such discrepancies do not affect our purpose much.

To lend additional support to our simulation results, we compared the simulated 10-m winds from the CTRL experiment with available observations at surface weather stations (Figure 5). At 0800 LST (Figures 5a and 5c), the observed and simulated winds over the northern HNI are both mostly southeasterly, although the observed wind speeds are noticeably weaker. By 1200 LST, winds over the northeastern part of the HNI strengthened in both observations and simulations (Figures 5b and 5d), with no substantial shift in wind direction except for the

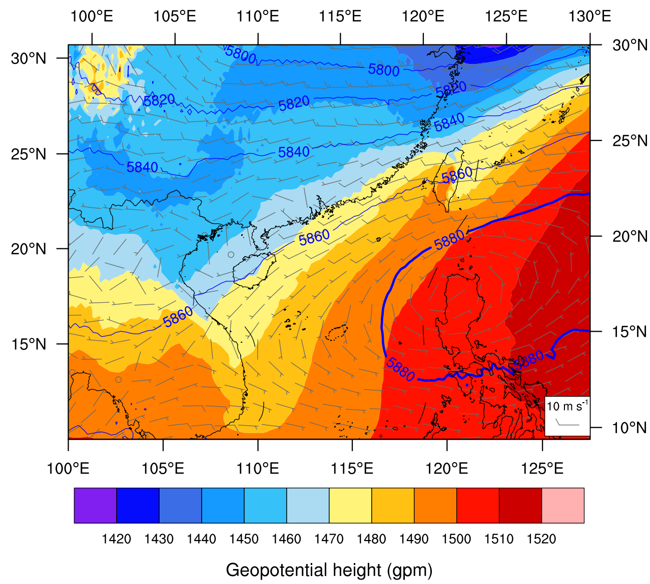

Figure 2. 500 hPa geopotential height (blue solid, contour interval = 20 gpm, with the line of 5,880 gpm thickened), 500 hPa wind barbs, and 850 hPa geopotential height (shaded) at 0800 LST 20 June 2017 based on NCEP FNL analysis.

winds in the northeastern part of the HNI away from the eastern coast (Figure 5d). The most prominent changes in wind direction in both simulation and observations occur over western-central northern HNI, where winds change from southeasterly to southwesterly and become stronger (Figures 5b and 5d), thereby gaining a cross-island westerly component along line A-B of Figure 1b. The wind direction changes in this part of the domain set up convergence near the center of the northern HNI (see the red dashed ellipses in Figures 5b and 5d), and the mechanism for the formation of the westerly wind component will be explained based on our simulation results. Therefore, the validity of the model simulated flow changes is supported by the available surface observations. In addition, the observed sounding profile at 0800 LST on 20 June 2017 from the Haikou radiosonde station, located near the northern coast of HNI (marked by the red cross in Figure 4a) is compared with the simulation. The vertical profiles of winds agree reasonably well, despite a slight underestimation of wind speed near 925 hPa (not shown).

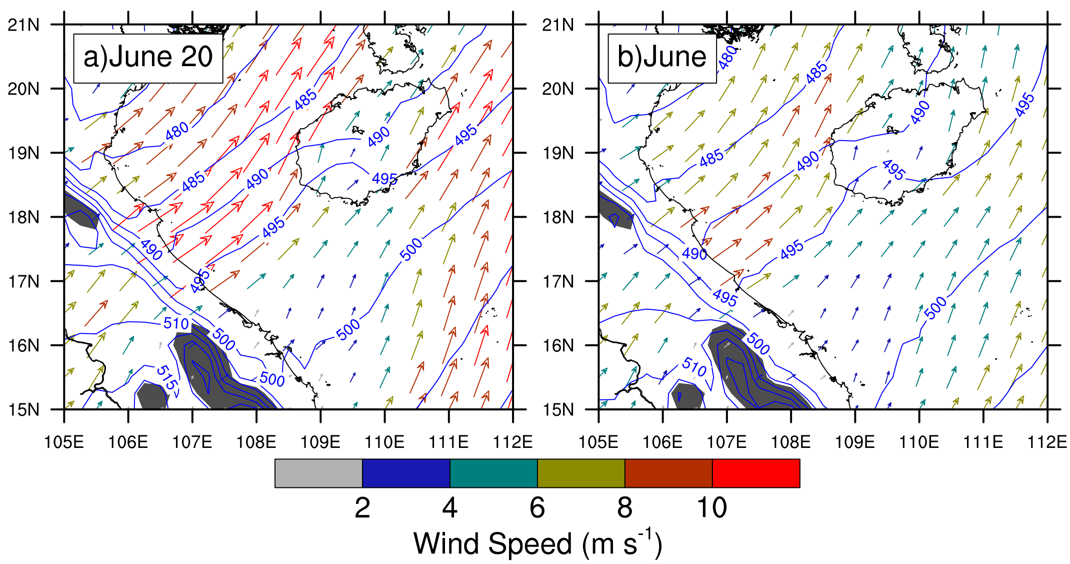

Figure 3. Average 950 hPa winds (colored by wind speed) and geopotential height (blue solid, contour interval = 5 gpm) (a) on 20 June 2017 and (b) in June from 2009 to 2018 based on ERA5 reanalysis. Dark gray represents the terrain height over 700 m.

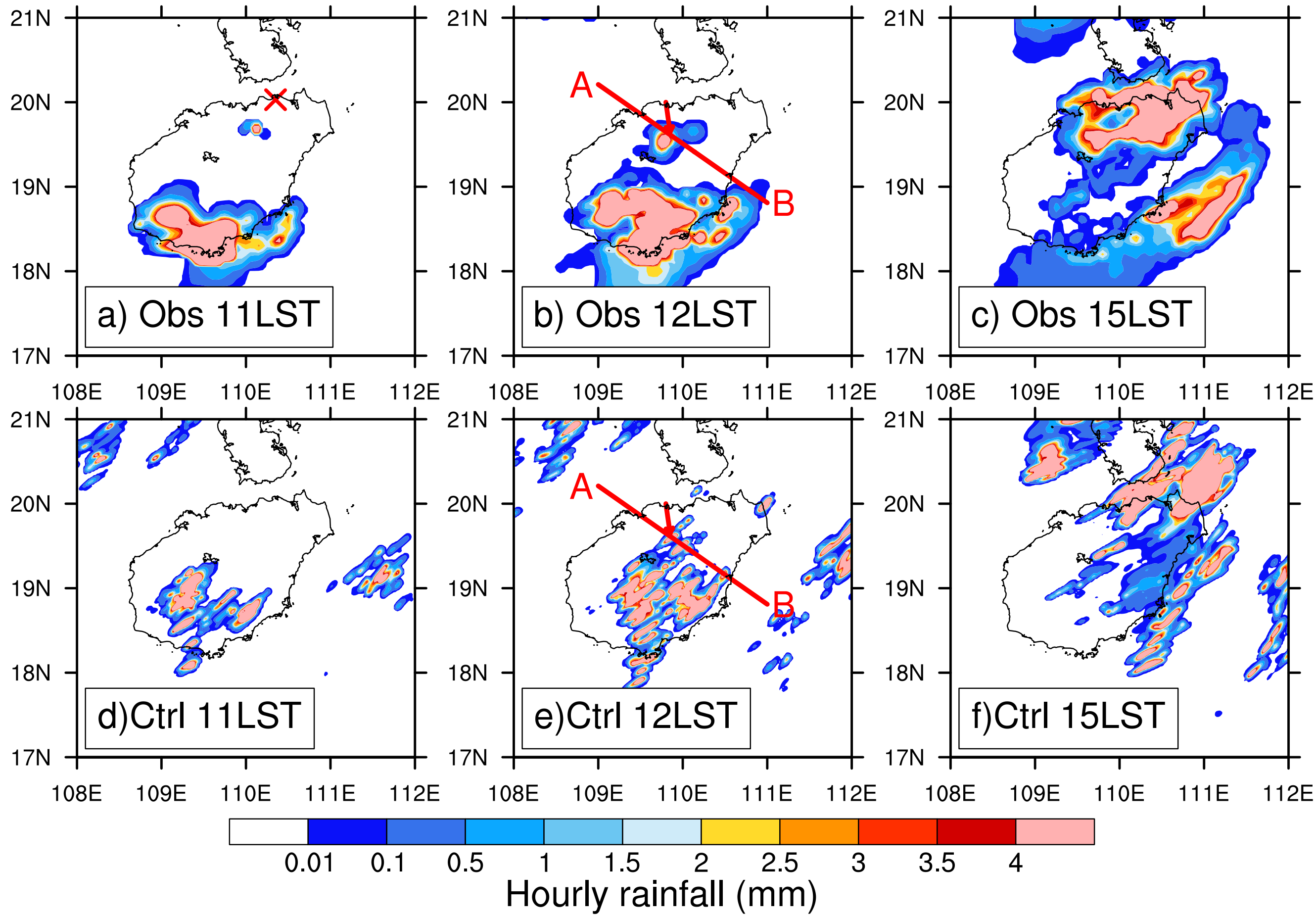

Figure 4. (a–c) Observed and (d–f) CTRL-simulated hourly rainfall (shaded) over HNI at 1100 LST, 1200 LST, and 1500 LST on 20 June 2017. The red cross in panel (a) denotes the Haikou radiosonde station. Lines A-B in panels (b, e) pass the rainfall initiation location marked by the red arrows.

Therefore, we believe that the CTRL simulation successfully captures the primary physical processes associated with the afternoon rainfall over the HNI and can thus be used to analyze the CI mechanisms.

4. CI Mechanisms of Afternoon Rainfall in Northern HNI

4.1. The Roles of Sea Breezes and BL Vertical Mixing in Rainfall Initiation

In general, sea-breeze fronts on the lee side of an island are a frequent trigger for rainfall because of the associated convergence near the fronts. This mechanism is what Zhu et al. (2017) and Liang and Wang (2017) proposed, who believe that the strong convergence tendency over the northern HNI is closely linked to enhanced sea-breeze fronts penetrating inland during the East Asian summer monsoon season. However, as discussed in the Introduction, when strong monsoonal southwesterly winds blow over HNI, sea breeze along the northern coast is difficult to advance inland, and those more capable of advancing inland should be from the island's west and east flanks, with the prevailing winds more or less parallel to the sea-breeze fronts. Line A-B (A: 20.21°N, 109.0°E, B: 18.81°N, 111.0°E) in Figures 1 and 4 is a line approximately perpendicular to the prevailing synoptic winds and the coastlines, and through the observed and CTRL-simulated CI locations. If sea breezes from the west and east coasts advance inland in the current case, there will be some indications along the line. Therefore, we will pay close attention to the wind components parallel to line A-B, that is, the northwesterly and southeasterly wind components, and their roles in convection initiation.

Figure 6 shows the 950 hPa winds before and at CI time over HNI and its adjacent seas, with the wind component projected onto line A-B within the displayed domain indicated by shading. The northwesterly component projected onto line A-B is positive and shown in warm colors, while the southeasterly component is in cold colors. At

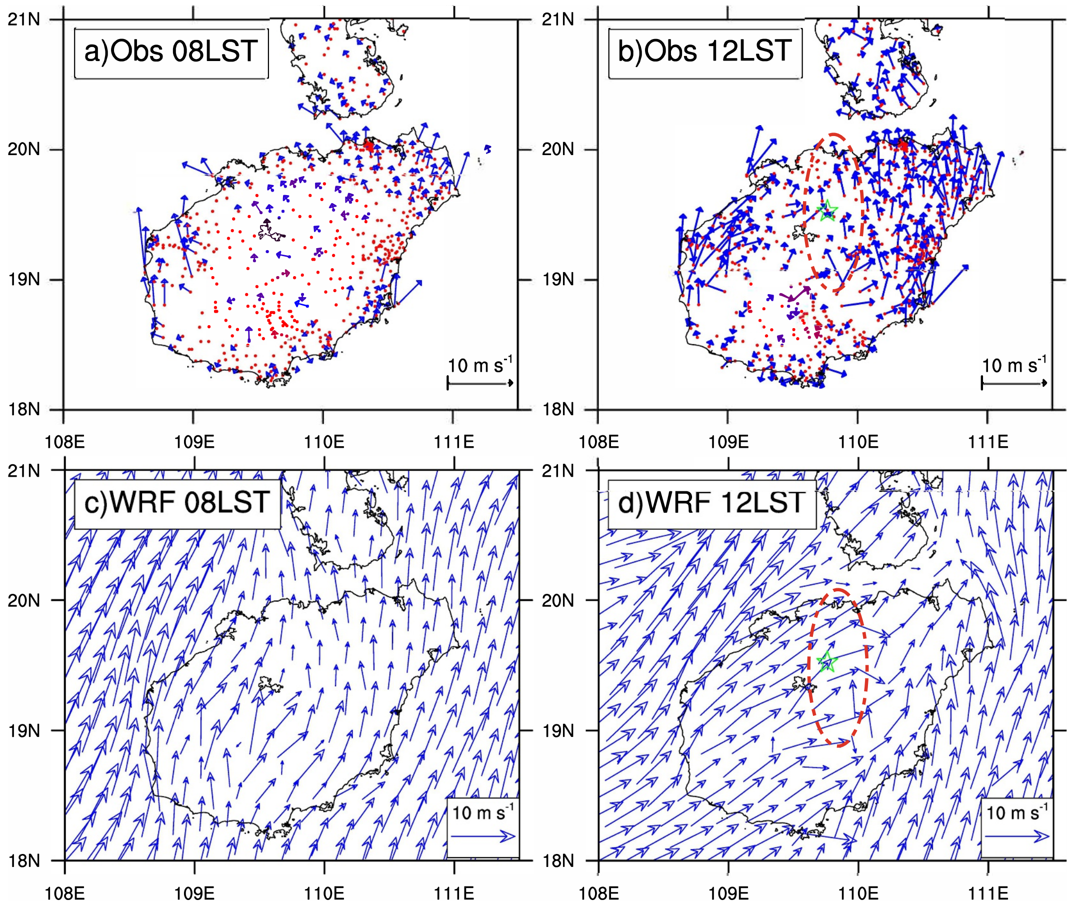

Figure 5. 10-m winds (blue vectors) at 0800 LST and 1200 LST on 20 June 2017, in automatic weather station observations (upper panels) and WRF CTRL simulations (lower panels). Red dots in panels (a, b) denote the locations of weather stations. The red dashed ellipses in panels (b, d) indicate the zone of low-level convergence in the observations and simulation, while the green star indicates where rainfall is first observed in the northern HNI.

0800 LST, the southeasterly component prevails over the entire island, except for some weak northwesterly winds on the northwest coast (Figure 6a). From 1000 LST to 1100 LST (Figures 6b and 6c), the northwesterly component increases rapidly and occupies most of the western island where southeasterly previously prevailed. With the enhancement of the northwesterly component, a convergence line is established in the inland area (Figure 6c), where the northwesterly component transitions to the southeasterly component along line A-B. By 1200 LST (Figure 6d), the northwesterly component on the western portion of the island is further enhanced, as is the southeasterly component. It leads to clearly stronger wind convergence where the two wind components meet on line A-B, which is also close to the location of convection initiation (indicated by the blue arrows in Figure 6d). At first sight, the convergence line, being roughly parallel to the east and west coasts, and located inland, resembles the convergence line between the sea-breeze fronts from opposite coasts when/if they collide. However, the time evolution of the convergence line is markedly different, as will be discussed next.

Based on the sea-breeze front collision mechanism (Zhu et al., 2017), northwesterly and southeasterly winds are expected to develop on the west and east coasts, respectively, and advance inland, colliding in the afternoon. To see if such processes occur, we examined the vertical cross-sections of winds, potential temperature/equivalent potential temperature, and total water-ice condensate along line A-B (Figures 7 and 8). At 1200 LST (see Figures 7d and 8d), the CI and associated significant updrafts (see the area enclosed by the white dashed ellipse in Figure 7d and the green stippled area in Figure 8d) occur near 110°E, where strong northwesterly winds on the left/west side of the panel converge with southeasterly winds on the right/east side. Meanwhile, the sea-breeze front on the west side stays near the west coastline and fails to penetrate inland, while that on the east side only progresses inland by about 20 km/~0.2° (see the cold front symbols below the abscissa in Figure 7d). Given

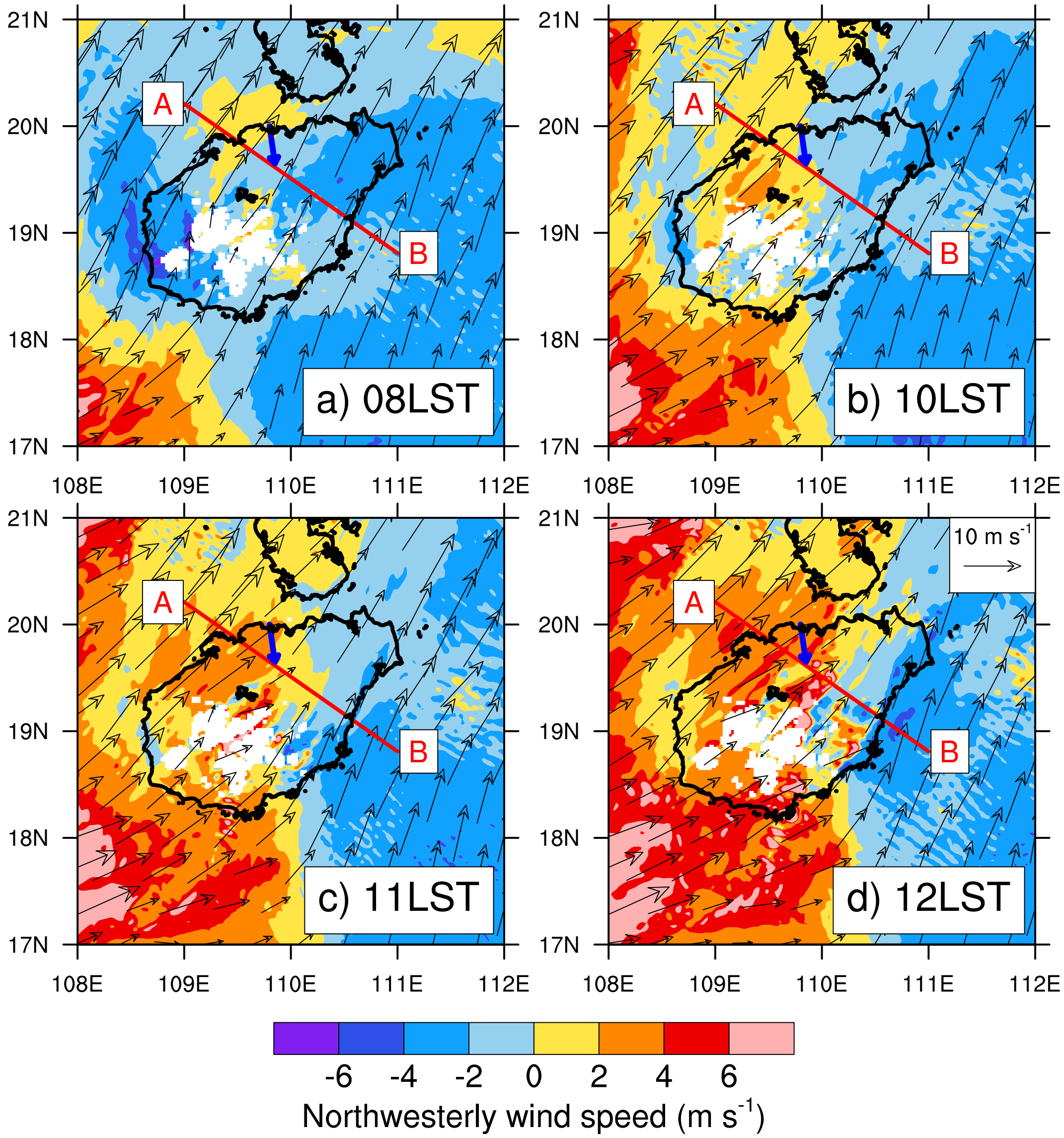

Figure 6. The black arrows (vectors) show the full horizontal wind field (direction and speed) at 950 hPa in CTRL, while the shading denotes wind components projected onto line A-B within the displayed domain (positive for northwesterly, negative for southeasterly). Panels correspond to (a) 0800 LST, (b) 1000 LST, (c) 1100 LST, (d) 1200 LST, 20 June 2017. Blue arrows indicate the location of rainfall initiation, consistent with the red arrows in Figures 4b and 4e.

the large distance between the two sea-breeze fronts and their distance from the inland CI location at this time, sea-breeze front forcing or the collision between them cannot be the reason for the CI near 1200 LST (see Figure 7d). Besides, when synoptic-scale southwesterly winds are strong, sea-breeze fronts from both the northwest and northeast coastlines are difficult to move inland, given the orientations of the coastlines (see Figure 6).

In the early morning at 0800 LST (Figure 7a), the lower levels within the cross section are dominated by the southeasterly wind component, with its depth increasing from about 500 m to about 1 km from the west to east side of the island, forming a wedge shape of the southeasterly wind component. The southeasterly wind component is stronger at the surface over the eastern part of the island. This overall pattern is consistent with the low-level flows shown in Figure 6a, which tend to turn westward when they pass over the island. The potential temperature (θ) field also shows upward-sloped isentropes that are more densely packed near the BL top, while air within the BL over land has lower θ. Over the western part of the island, the BL is much shallower, and the

10.1029/2025JD045812

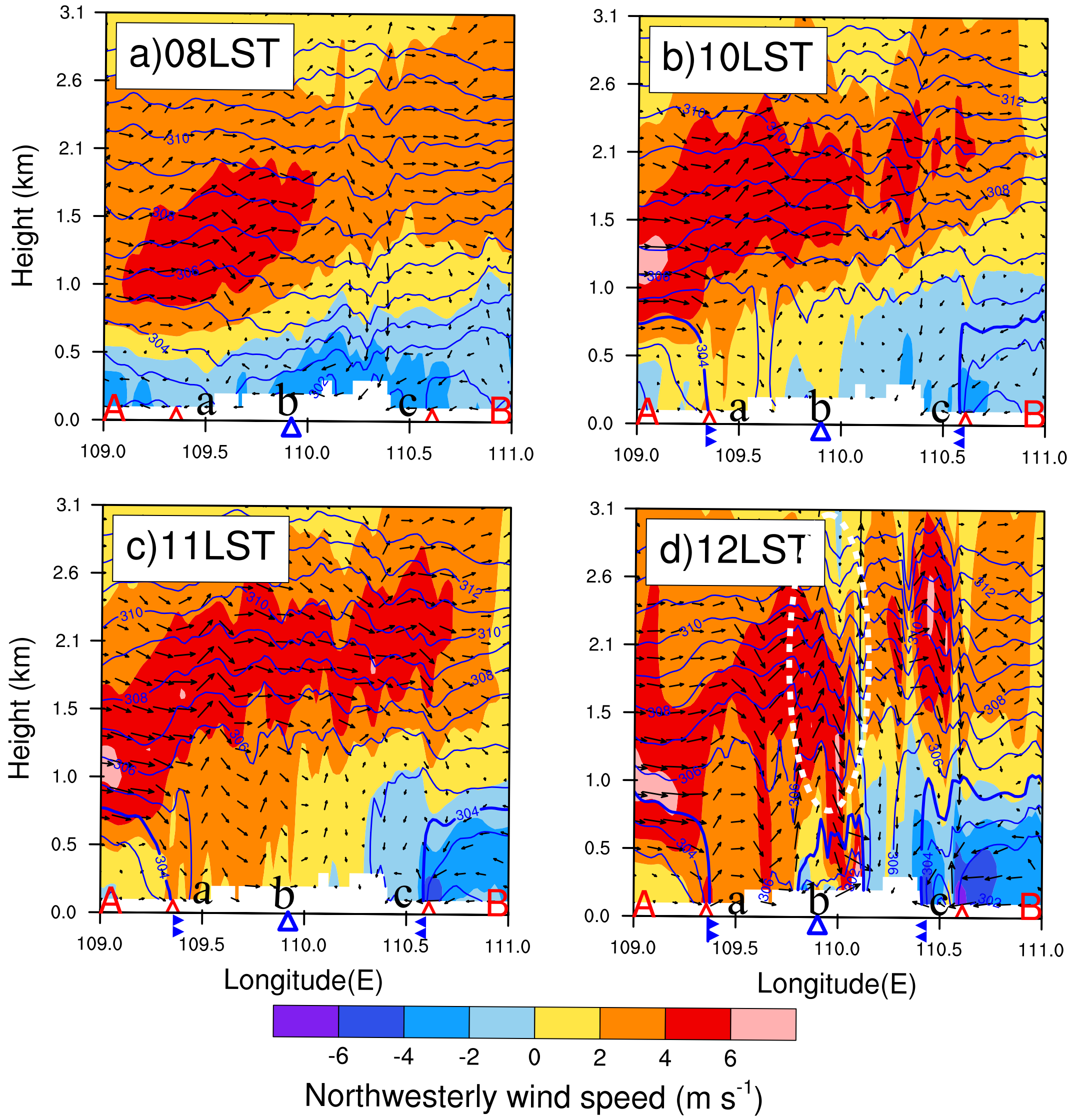

Figure 7. CTRL-simulated potential temperature (blue solid, contour interval = 1.0K), horizontal wind component (shading, positive for northwesterly and negative for southeasterly), and wind vectors projected onto the cross-section A-B in Figure 6 with the vertical component amplified by a factor of 10 at (a) 0800 LST, (b) 1000 LST, (c) 1100 LST, (d) 1200 LST, 20 June 2017. The thick blue temperature contours outline the leading sea-breeze frontal surface or outflow boundary; the white dashed ellipse in panel (d) marks the significant updrafts; the red triangles on the abscissas mark the west and east HNI coastlines. The blue triangles below the abscissas mark where CI occurs are the same as the arrows in Figures 4 and 6, and the cold front symbols indicate the locations of sea-breeze fronts. Labels a, b, and c on the abscissa indicate the locations of vertical profiles shown in Figures 9 and 10.

northwesterly wind component is stronger at the same height levels, reaching over 4 m s^{-1} above 1 km. Besides, because equivalent potential temperatures (θ_e) decrease with height over the island (see Figure 8a), the air is potentially unstable since 0800 LST, similar to the air over the neighboring sea. Contrary to the θ field, θ_e shows that the air over the east island is warmer instead (cf. Figures 7a and 8a), indicating more water vapor content in the island's east. The cause of drier air in the western part will be analyzed later.

By 1000 LST (Figure 7b), much of the strong vertical gradient of θ has been eroded by BL vertical mixing, making the BL θ more or less uniform up to 1 km. The strongest horizontal gradients of θ are now found near the east and west coastlines, where the sea-breeze fronts are located. Given the wedge shape of the southeasterly wind component earlier on (see Figure 7a), the western portion of the southeasterly winds at the low levels is first eroded and replaced by the northwesterly component at the surface over land (Figure 7b), and west of 109.7°E, the

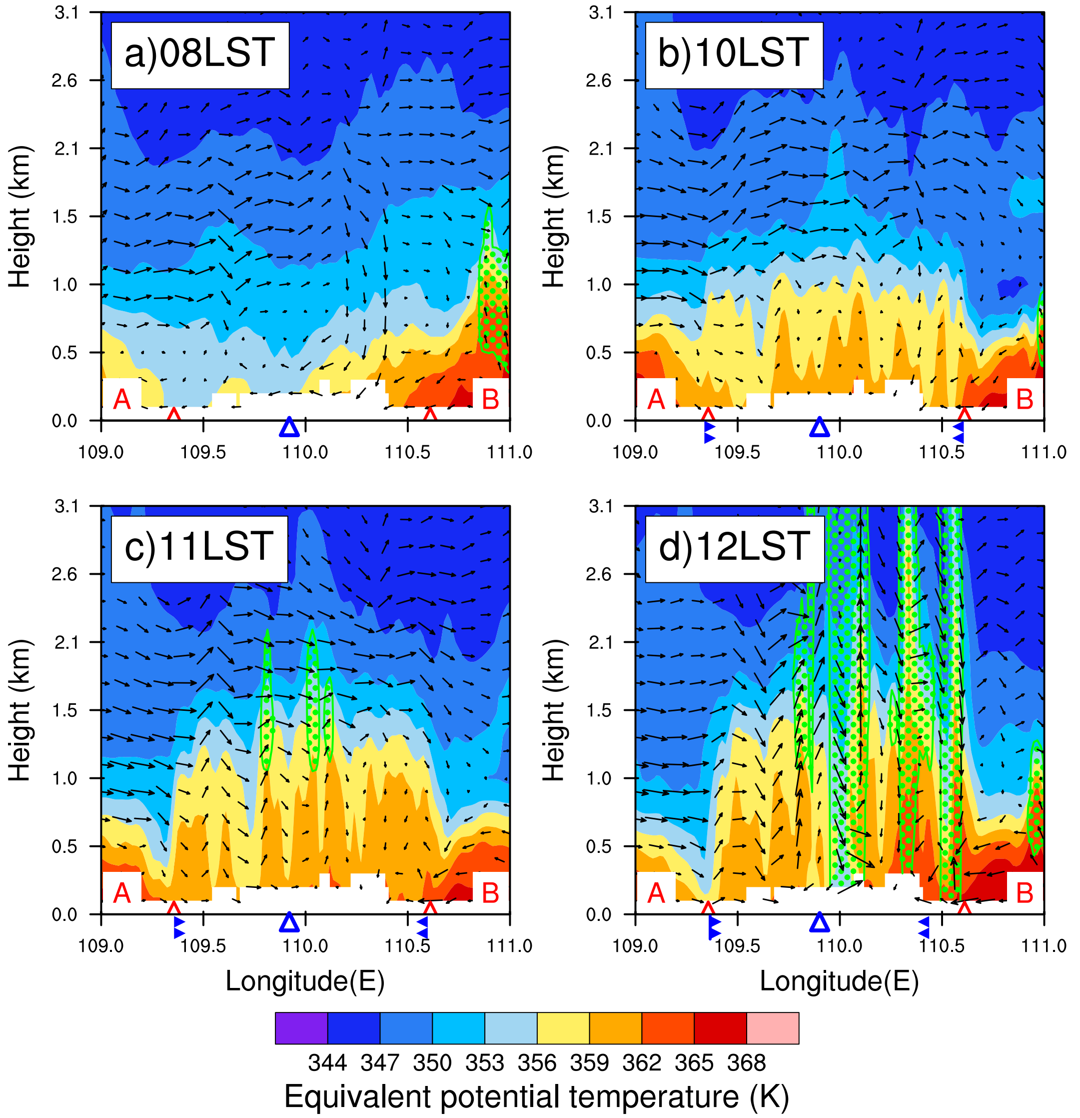

Figure 8. CTRL-simulated equivalent potential temperature (shading), the 0.01 g kg^{-1} total water-ice condensate (the green solid lines stippled inside outlining the clouds) and wind vectors projected onto cross-section A-B shown in Figure 6 with the vertical component amplified by a factor of 10 at (a) 0800 LST, (b) 1000 LST, (c) 1100 LST, (d) 1200 LST, 20 June 2017. Labels and marks on/below the abscissas are the same as in Figure 7.

significant northwesterly component extends from the ground level up all the way and connects with the strongly northwesterly winds above. This northwesterly wind component is ahead of the west coast sea-breeze front and is clearly created by downward moment transport via BL vertical mixing. The result is the setup of a convergence zone between the northwesterly and southeasterly wind components through the depth of the BL at ~109.7°E within this cross section, which extends north and south further away from the cross section to form a convergence line (see Figures 6b and 6c). Meanwhile, in the θ_e field (Figure 8b), the potential instability over the island is enhanced by BL heating in the absence of observable updrafts or cloud formation at this time.

One hour later, by 1100 LST, the well-mixed BL further develops to reach ~1.3 km MSL (Figure 7c). The northwesterly wind component over the western part of the island is now over 2 m s^{-1}, and the leading edge of the 2 m s^{-1} northwesterly wind is at ~109.9°E. The two sea-breeze fronts remain close to the coastlines. At the same time, clouds start to appear on the top of the BL near 109.9°E due to weak updrafts in the convergence zone (see the green stippling in Figure 8c). By 1200 LST (Figure 7d), the northwesterly wind component on the west side of the convergence zone is enhanced further, reaching over 4 m s^{-1} immediately behind the convergence zone. A

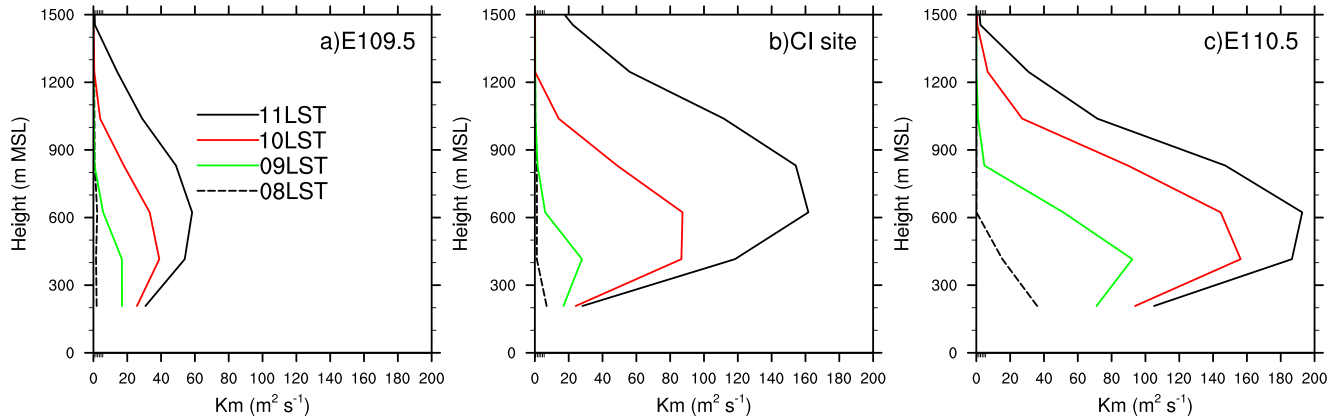

Figure 9. Vertical profiles of K_m (eddy diffusivity for momentum) in the BL during 0800–1100 LST on 20 June 2017 at the locations (a–c) along cross-section A-B (see Figure 7) (a) at 109.5°E near the west coast, (b) near but west of the CI location (see the blue triangles below the abscissas of Figure 7), and (c) at 110.5°E near the east coast.

deep convergence zone extending to 1.5 km MSL is present at this time while the isentropes exhibit an apparent upward bulge on the west side of the convergence zone, indicating persistent upward lifting of potentially unstable air in the BL (see Figures 7d and 8d). Clearly, it is such persistent convergence lifting rather than the sea-breeze front circulations that initiates the convection at this central island location (see the strong updrafts and deep clouds at ∼109.9°E in Figures 7d and 8d). The deeper layer of southeasterly flow component on the east side of HNI and the relatively shallow layer on the west side, combined with the stronger above-boundary-layer northwesterly wind component in the early morning, help set up a strong BL convergence zone. The wedge shape and the differential depth of the initial southeasterly flow component setup resembles the BL of varying depth over the sloping terrain of western Texas and Oklahoma, where the erosion of shallower BL on the west side by BL vertical mixing and downward transport of westerly momentum create strong convergence along a dryline, and initiate convective storms along the dryline (Xue & Martin, 2006a, 2006b). There are strong similarities in the fundamental physical mechanisms between these two phenomena, despite their very different geographic and synoptic settings.

To lend support to our proposed mechanism in which the low-level convergence near the CI location is said to be created by BL vertical momentum mixing as described above, we plot the vertical profiles of momentum eddy diffusivity coefficient, K_m, that is part of the PBL parameterization scheme, at 0800, 0900, 1000 and 1100 LST on 20 June 2017 in Figure 9. The profiles are at the three points west, near but west, and east of the CI location along cross-section A-B, as indicated by labels a, b, and c in Figure 7.

A clear temporal evolution is observed in the K_m profiles (Figure 9). The vertical mixing in the BL, negligible at 0800 LST, becomes prominent by 1100 LST at all three locations. Spatially, the mixing is stronger near the east coast (110.5°E; Figure 9c), somewhat weaker near but west the CI location (Figure 9b) and significantly weaker near the west coast (109.5°E; Figure 9a). The increase in K_m is due to daytime surface heating and the development of unstable convective boundary layer with strong turbulence mixing. The larger K_m values on the east side are consistent with the weaker vertical stratification at the lower levels, as indicated by the vertical potential temperature gradient in Figure 7.

The upper panels of Figure 10 show the vertical profiles of the northwest-to-southeast component of wind along cross-section A-B at the three locations, at 0800 and 1100 LST, while the lower-panels of Figure 10 plot the total change in that wind component from 0800 to 1100 LST together with the accumulated changes produced by vertical momentum mixing, as calculated by the PBL scheme. The latter quantifies the amount of momentum change due to mixing.

We can see that near but west of the CI location, the easterly wind component at 0800 LST below ∼600 m is changed to positive values by 1100 LST while the westerly wind component at the upper boundary layer is reduced (Figure 10b), and such increases and decreases are consistent with large positive and negative changes due to turbulence mixing (Figure 10e). The effect of vertical mixing is to make the wind speed more uniform

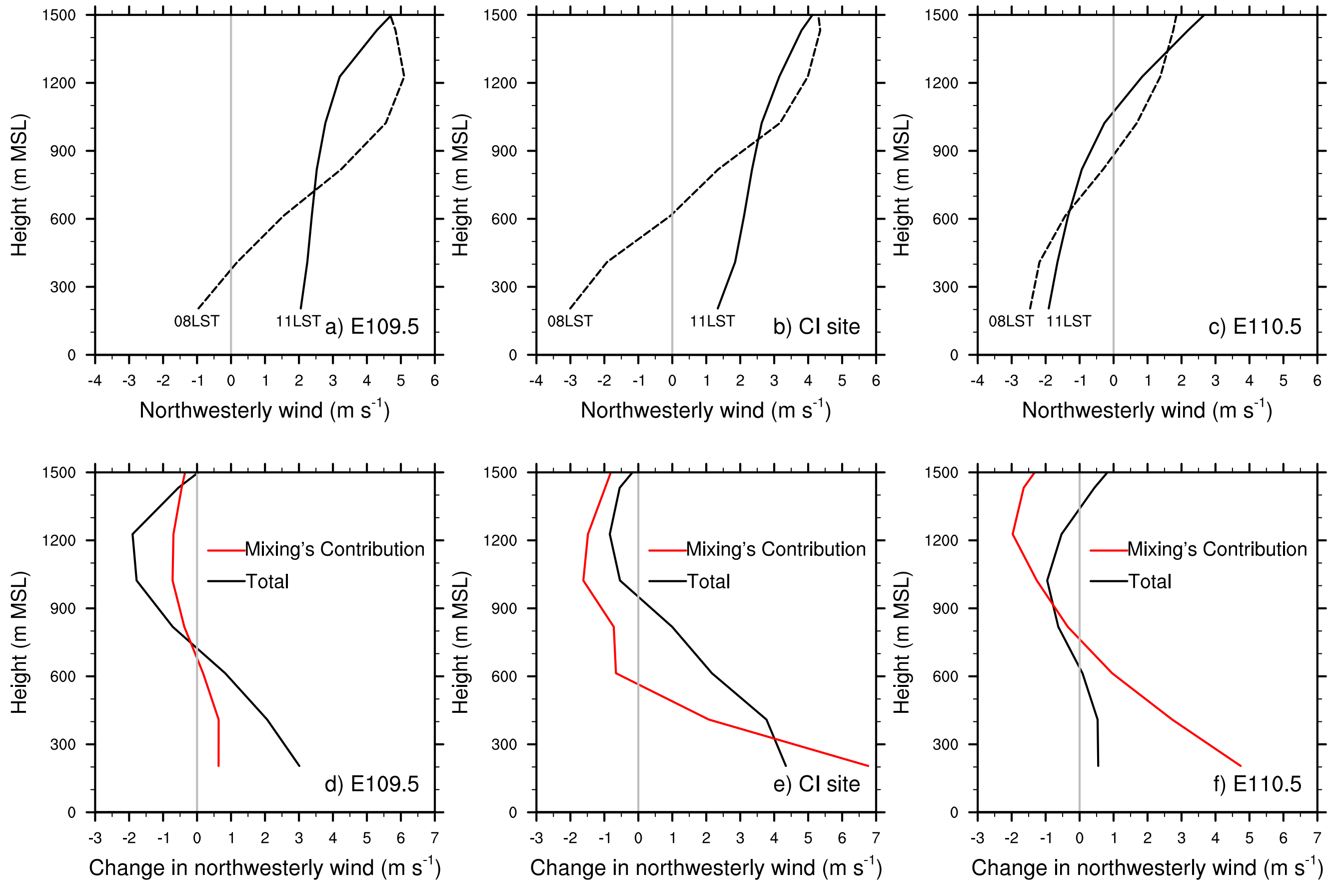

Figure 10. Upper panels: Vertical profiles of the BL northwesterly wind component along cross-section A-B (see Figure 7; positive values denote northwesterly winds, negative values denote southeasterly winds) on 20 June 2017 (a) at 109.5°E near the west coast, (b) near but west of the CI location (see the blue triangles below the abscissas of Figure 7), and (c) at 110.5°E near the east coast for 0800 LST (dashed lines) and 1100 LST (solid lines). Lower panels: Vertical profiles of the total change in northwesterly winds (black lines) and the contribution of vertical mixing (red lines) between 0800 and 1100 LST on 20 June 2017 along cross-section A-B (positive values indicate northwesterly wind enhancement, negative values indicate northwesterly wind reduction) at the three points.

throughout the depth of the boundary layer (Figure 10b), and near the surface, the effect of the mixing enhancement to the westerly wind component is actually reduced somewhat, likely by surface drag (Figure 10e).

Near the west coast at 109.5°E, the vertical uniformization of the wind is also clearly evident (Figure 10a), although Figure 10d suggests that mixing accounts for only part of the change. The additional changes, with an increase in westerly and easterly flows at the lower and upper levels, respectively, are consistent with the sea-breeze circulation near the west coast. Near the east coast at 110.5°E, vertical mixing again caused a significant increase in low-level and decrease in upper BL northwesterly winds (red line in Figure 10f). However, the total changes (black line in Figure 10f) are much smaller. This should be because the changes due to mixing are significantly offset by the sea-breeze circulation, that is, easterly at the lower-levels and westerly at the upper levels.

The above results clearly indicate that vertical mixing plays dominant roles in boundary layer wind changes, especially near the CI location at the center of the northern Hainan Island. The sea-breeze circulations near the west coast and east coast increase and decrease the mixing change tendencies, respectively, but given that the sea-breeze fronts at the CI time are still far from the CI location (Figure 7d), the effects of sea-breeze circulations on the CI should be negligible. The low-level convergence created by the vertical momentum mixing, by bringing the westerly flow components from a lower elevation on the west side of CI location to the surface, is primarily responsible for initiating the convection there. As the northwesterly momentum west of the CI location is transported downward to the surface, the northwesterly winds oppose the southeasterly flows that have yet to be eroded by the mixing east of the CI location (Figures 7b–7d), and strong low-level convergence is created near the central part of the island, and such convergence triggers convection and produces subsequent rainfall.

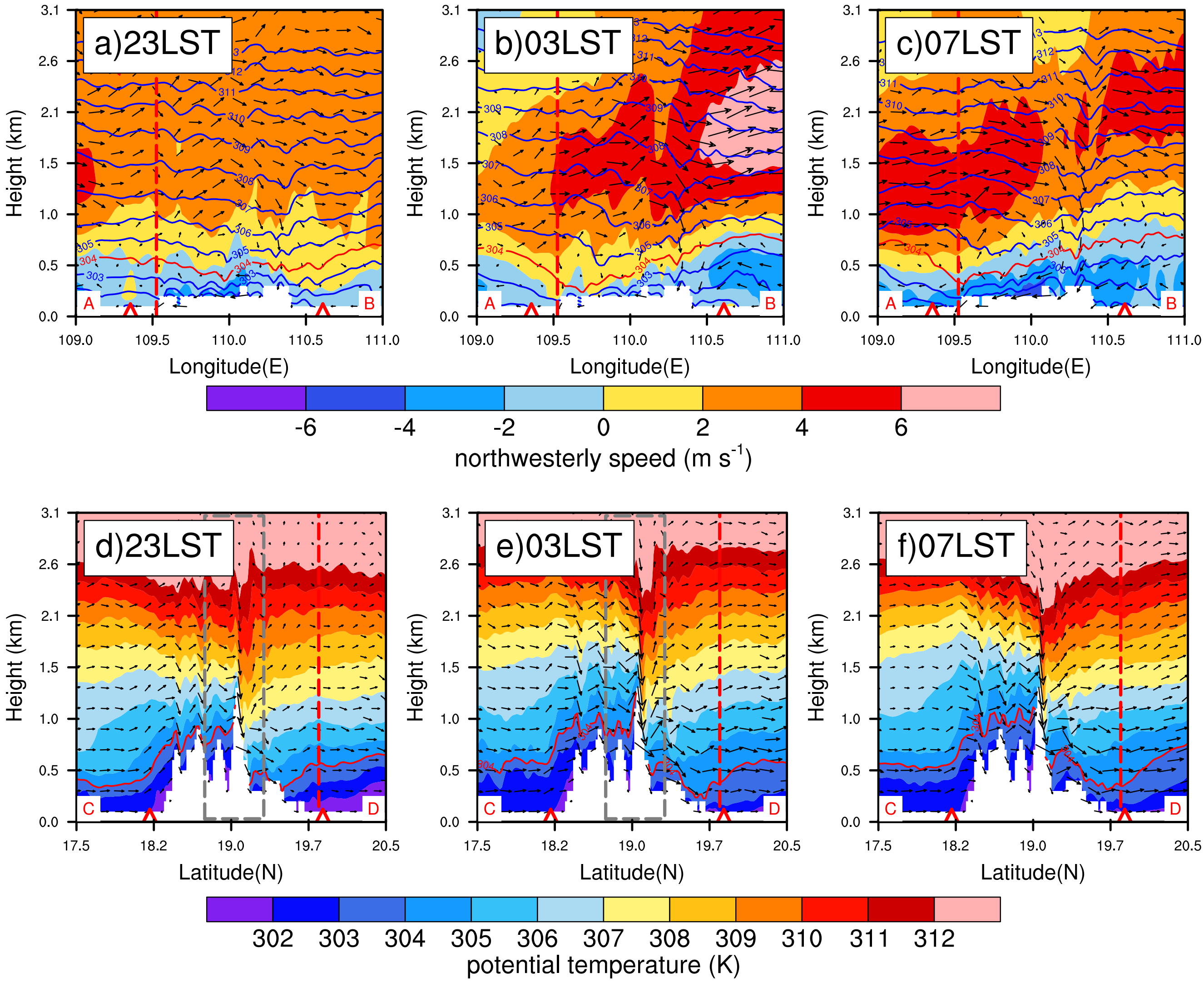

Figure 11. Upper panels: The same as Figure 7 but at (a) 2300 LST 19 June, (b) 0300 LST, and (c) 0700 LST, 20 June 2017. Lower panels: CTRL-simulated vertical cross sections of potential temperature (shaded) and wind vectors projected onto cross-section C-D shown in Figure 1b at (d) 2300 LST 19 June, (e) 0300 LST, and (f) 0700 LST, 20 June 2017. In all panels, the vertical component of wind vectors is amplified by a factor of 10, with red solid lines denoting the 304K potential temperature contours. Triangles on the abscissas mark the coastlines of HNI, and vertical red dashed lines indicate the intersection of cross-sections A-B and C-D (see Figure 1b). Gray dashed boxes in panel (d) and (e) denote the region to be presented in Figure 12.

4.2. The Formation of the Wedge-Like Southeasterly Wind Structure

The development of the BL convergence zone, discussed earlier, is closely linked to the unique wedge-like structure of BL winds in the morning, where the southeasterly wind component undercuts the northwesterly wind component aloft (see Figure 7a). With such a structure, the shallower BL with the southeasterly wind component on the west side can be more quickly eroded by BL vertical mixing, creating a convergence zone between the deeper southeasterly winds to the east (see Figures 7b and 7c). Then, the question is: How is this wedge-like wind structure established?

To address this question, we present the vertical cross-sections in Figure 7 along line A-B prior to 0800 LST (Figures 11a–11c). At 2300 LST, 19 June 2017 (Figure 11a), the low-level southeasterly wind component is of similar depth over the island, and the air on the west side is slightly colder with 304K at about 600 m MSL (see the intersection between the red dashed line and the 304K contour in Figure 11a). By 0300 LST, the isentropes are noticeably depressed downward on the west side, for example, the contour of 304K descends to about 300 m MSL, causing the air there to be warmer than that on the east side; meanwhile, the wedge-like wind structure emerges

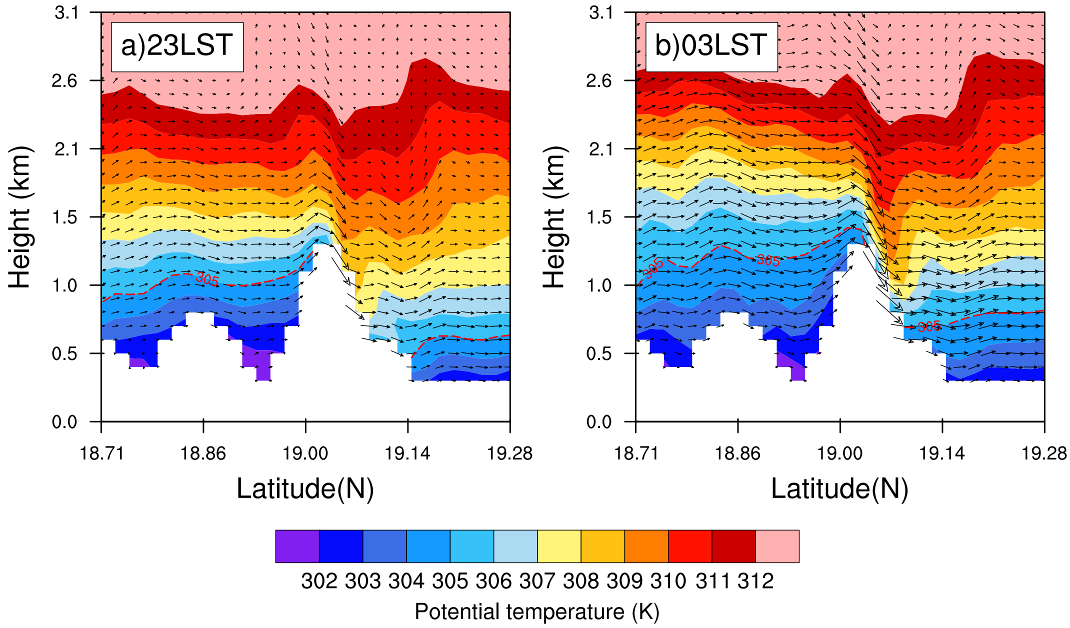

Figure 12. Zoomed-in views of the dashed gray boxes in Figures 11d and 11e for (a) 2300 LST 19 June and (b) 0300 LST 20 June 2017. The dashed red contours are 305K potential temperature.

(Figure 11b). By 0700 LST (Figure 11c), the wedge-like structure and the sloping isentrope pattern had fully developed, closely resembling those at 0800 LST (cf. Figures 7a and 11c). Consequently, we can infer that the wedge-like wind structure forms after midnight and should be closely related to the downward depressed isentropes on the west island. This should not be due to the northwestward advection of nighttime radiatively cool air on the east side of the island because that process should make the air colder on the downwind or the west side of the island.

The natural follow-up question is then: what causes the downward depression of the isentropic surfaces after midnight through early morning on the west side of northern HNI? We hypothesize that the mountains in southern HNI, situated along the path of the prevailing flows to the northwest part of the island (see Figure 6a), play a crucial role. The nighttime stable BL air in the prevailing south-southwesterly flow can climb over the southern mountains and descend along the lee slope in the form of downslope winds, eventually restoring to higher levels in the form of a hydraulic jump further downstream (Durran, 1986). Such processes of strong downslope flow and subsequent hydraulic jump were also reported to occur in the lee of the eastern coastal mountains of the ICP at night, as noted by Wang et al. (2022).

To confirm our hypothesis, we present the vertical sections across the southern mountains in a south-north orientation along line C-D in Figures 1b and 11d–11f. At 2300 LST, the flows on the lee slope are still relatively weak (Figure 11d). With time, the flows strengthen notably on the lee slope and over the mountain top at 0300 and 0700 LST (Figures 11e and 11f). With the enhancement of descending flows, the potential temperature contours become steeper on the lee slope, with the 304K isentrope descending from above 600 m to below 300 m (Figures 11e and 11f), in line with the height of 304K in cross-sections A-B (Figures 11b and 11c).

Figure 12 shows close-up views of the gray dashed boxes in Figures 11d and 11e, centered on the highest mountain, to determine whether the low-level flows climb over it. At 2300 LST, the air at a temperature of 305K is blocked by the mountain. However, at 0300 LST, with the enhancement of winds on the windward side, it climbs over the mountain and descends drastically along the lee slope. This confirms that the strong downslope winds on the lee slope are indeed due to the flows crossing over the mountains. The downward sloping of the isentropes corresponds to the downward dipping of the isentropic surfaces, as well as the downward transport of higher momentum from above. This also explains the presence of the drier air in the island's west that we observed in Figure 8a.

Regarding the acceleration of winds from midnight to early morning on the windward side of the HNI, our previous study showed a nocturnal peak in the diurnal variations of 925 hPa winds in the upstream region (see

10.1029/2025JD045812

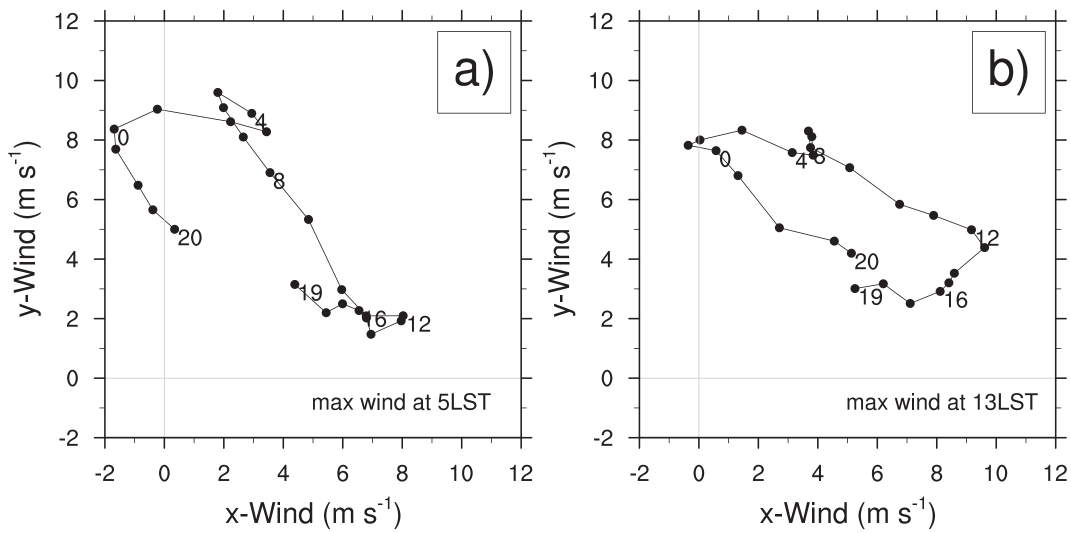

Figure 13. Diurnal variations of 950 hPa wind vectors (a) at point C and (b) at the south coastline (see point C and the left triangle on the abscissa of Figure 11d for the specific locations) from 2000 LST 19 June through 1900 LST 20 June. Dots on the curves and numbers beside them are the tips of wind vectors from the coordinate origin and the corresponding local times, for example, "20" for 2000 LST 19 June, "0" for 0000 LST 20 June, and so forth. Labels in the lower right corner of the panel indicate the times when the winds peak.

Figures 8c and 8d in Wang et al. (2022)). Here, we present the hodographs of 950 hPa winds at an upstream offshore point C and a windward coastline point (see Figures 1b and 11d–11f), respectively, in Figure 13. It reveals that the 950 hPa winds also have a nocturnal peak (0000–0500 LST) as well as a near-noon peak (1200–1300 LST). However, unlike the near-noon peak characterized by significant westerly winds, the nocturnal peak is primarily characterized by southerly winds (see Figure 13).

After analyzing the 950 hPa diurnal perturbed winds (see Figure 14), we find that there are prominent southeasterlies on the sea upstream of HNI at 0200 LST (see Figure 14b). These perturbed southeasterlies combine with the environmental southwesterlies (Figure 3a), thereby strengthening the southerly winds at night. The enhancement of southerly winds makes it easier for the flows to climb over the mountains in the early morning, producing stronger downslope flows in the lee.

Concerning the perturbed southeasterlies upstream of HNI at 0200 LST (Figure 14b), they are most likely advected from the ICP coast on the previous night or 2000 LST (Figure 14a), similar to the mechanism advocated by Wang et al. (2022), and rather than being due to physical processes on HNI, such as land or sea breeze. Furthermore, the upstream perturbed southeasterlies are inherently ageostrophic and would rotate clockwise during advection due to inertial oscillations (Blackadar, 1957) (see the winds in the cold shading area in Figures 14a and 14b). A similar phenomenon also occurs during the daytime when notable perturbed northwesterly winds from the ICP coast are advected downstream while rotating clockwise as well (see Figures 14c and 14d).

We also calculated the Froude number of flows at 333 m above ground level (AGL), the fourth-lowest model level, over the adjacent sea, using an assumed terrain elevation of 951 m (Figure 15). Although 951 m is only half the elevation of the highest peak (1,867 m), most mountainous areas over HNI do not exceed this height, except for a few isolated peaks (see Figure 1b). Thus, using 951 m as a representative mountain elevation is reasonable.

Based on Figures 15a–15c, the Froude number upstream of HNI remains below 1.0 from the previous afternoon to early evening and exceeds 1.0 from late evening to early morning. This transition occurs near midnight, coinciding with the enhancement of southerly flows, indicating a shift from predominantly flow-around to flow-over conditions. The results also show that upstream flows approaching the western section of the southern HNI coast exhibit a higher Froude number, implying that more of these flows can climb over the terrain and descend toward the northwestern part of the island on the lee side.

The above processes can also be seen in the evolution of the 304K isentropic surface on the northern HNI (Figures 15d–15f). At 2000 LST in the early night (Figure 15d), the 304K isentropic surface slopes upward from

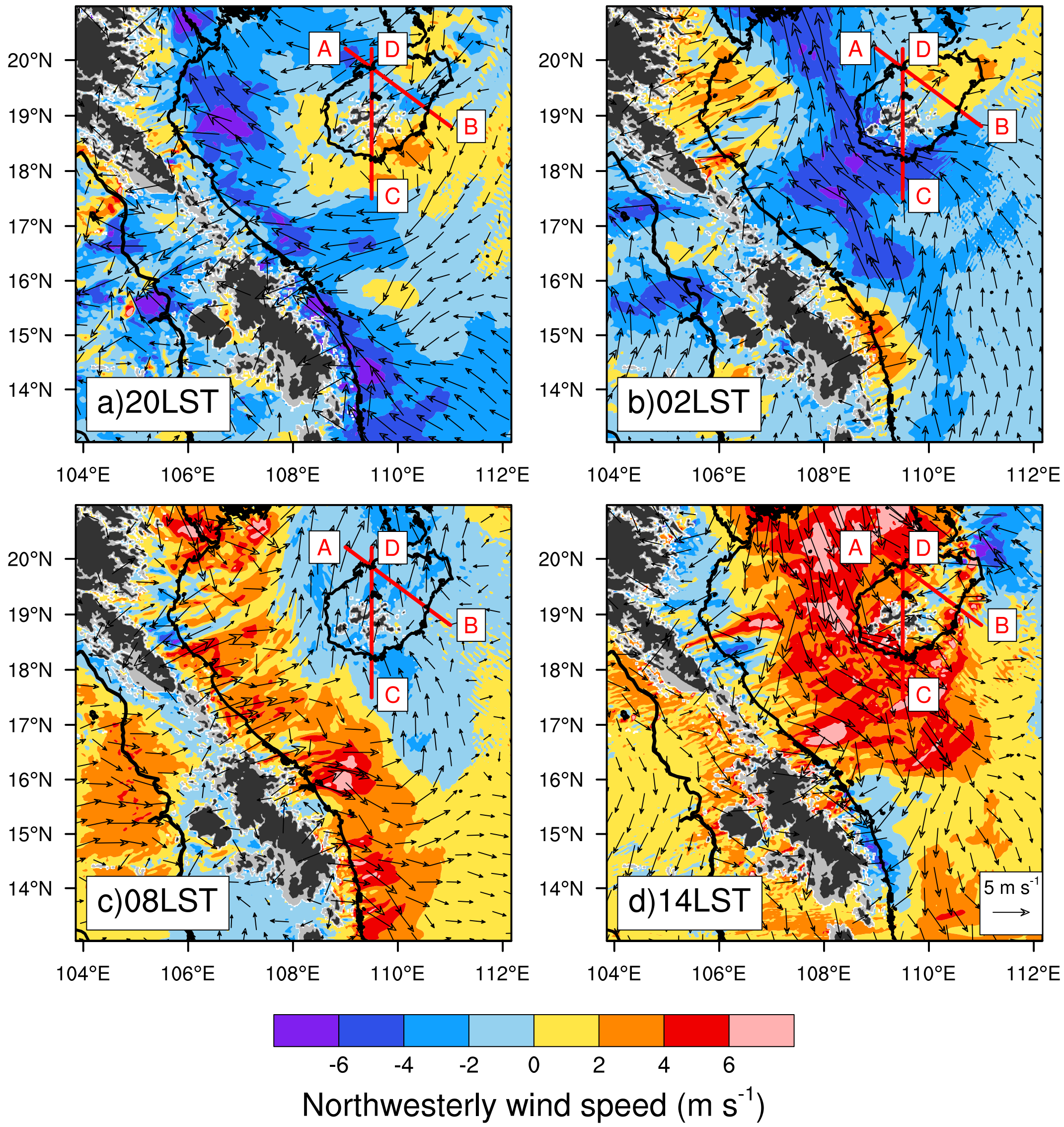

Figure 14. The black arrows (vectors) denote 950 hPa perturbation winds relative to the daily mean from the CTRL run at (a) 2000 LST 19 June, (b) 0200 LST, (c) 0800 LST, and (d) 1400 LST 20 June 2017. Shading shows the wind component projected onto line A-B, with warm colors representing northwesterly winds and cold colors representing southeasterly winds. Light gray and dark gray shading denote terrain elevations above 500 and 700 m, respectively. Lines A-B and C-D are consistent with those in Figure 1b.

below 200 m further upstream to above 500 m near the southern coast of HNI. On the windward slope of the mountains, the surface reaches over 900 m, but dips below 400 m on the immediate leeward slope. Similar patterns are also seen at 2300 LST (Figure 15e), but the isentropic surface dips below 300 m on the lee slope further downstream. At these times, there are also significant around-mountain flows on the west side of the mountains, which can contribute to the enhancement of the westerly wind component when the around-mountain flows try to restore back toward the central axis of flow on the lee side.

At 0300 LST (Figure 15f), the 304K isentropic surface is elevated significantly on the windward slope, whereas on the lee side, the area where the surface dips below 300 m shifts further downstream close to the coastline. This is clearly related to the enhancement of the upstream flow and might have also been helped somewhat by the radiative cooling on the mountain slope, but the latter should be secondary. The reason that the 304K isentropic surface drops less in the eastern part of the northern HNI should be mainly due to the lower mountain height over the southeastern HNI (see Figure 1b). By 0700 LST (not shown), the pattern of 304K isentropic surface in the lee,

10.1029/2025JD045812

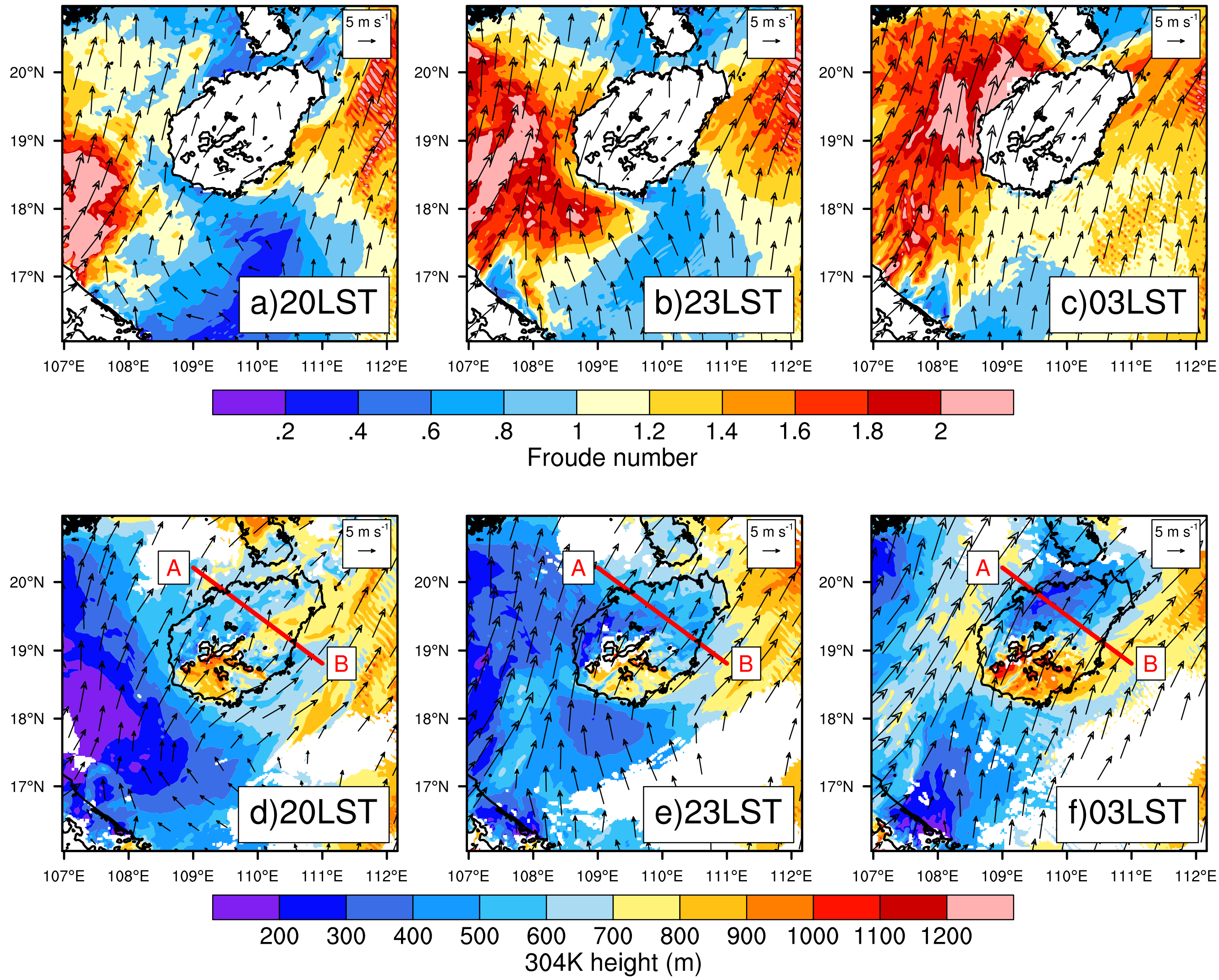

Figure 15. Upper panels: Froude number (shaded, only displayed over the ocean) and horizontal wind vectors at ~333 m AGL, assuming a mountain altitude of 951 m, at (a) 2000 LST, (b) 2300 LST 19 June 2017, and (c) 0300 LST 20 June 2017. Lower panels: Height of the 304K isentropic surface (shaded) and wind vectors along the 304K isentropic surface at (d) 2000 LST, (e) 2300 LST 19 June 2017, and (f) 0300 LST 20 June 2017. Line A-B, consistent with prior figures, illustrates the spatiotemporal evolution of the isentropic surface.

which is more downwardly depressed in the west, becomes full-fledged, corresponding to the wedge-like southeasterly wind structure in Figure 11c, given that the isentropic surfaces also divide the atmosphere into layers with possibly different momentum.

In short, BL vertical mixing and unique wedge-like wind structures are the key factors for the CI in north central HNI. Sea-breeze fronts from the northeast and northwest coastlines do not appear to be important factors here. The formation of the wedge-like wind structure is closely related to the nocturnal acceleration of wind upstream of the HNI and the mountains over southern HNI. Next, we will present the results of sensitivity experiments to further support our conclusions.

4.3. Results of Sensitivity Experiments

4.3.1. Convection Initiation in the Absence of BL Vertical Mixing in FixTSK Experiment

In experiment FixTSK, the surface skin temperature (TSK) on HNI is fixed to the value at the model's initial time, 0800 LST on 19 June 2017. In the absence of radiative heating-induced surface temperature increase during the day, BL vertical mixing is mostly suppressed over HNI. Here, Figure 16 presents the same vertical cross-section

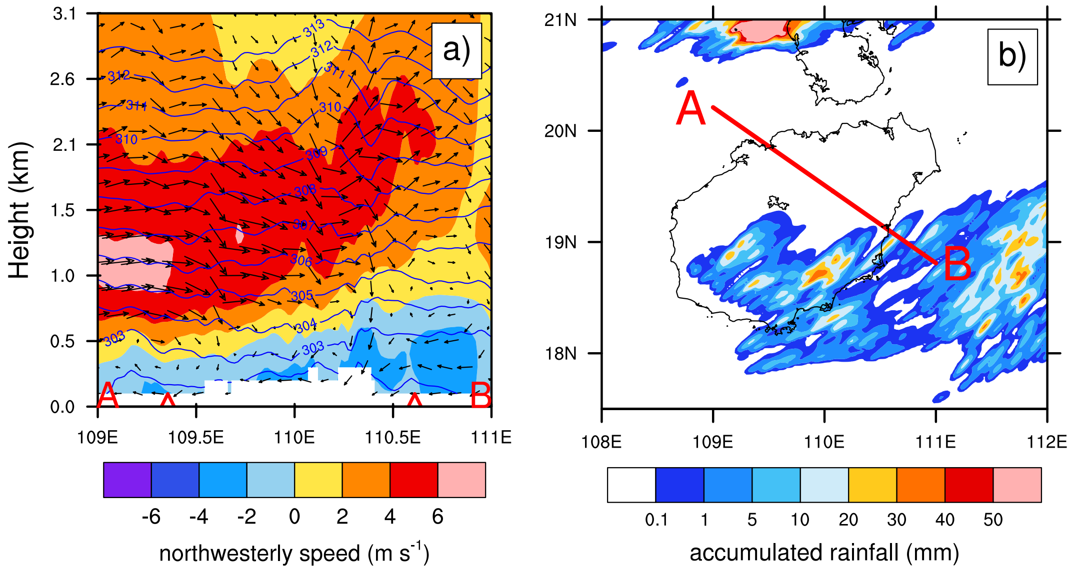

Figure 16. (a) Same as Figure 7 but for 1200 LST 20 June in FixTSK and (b) 12-hr accumulated rainfall from 0800 LST to 2000 LST 20 June in FixTSK.

A-B as shown in Figure 7, along with the accumulated rainfall over HNI during the daytime of 20 June 2017 for FixTSK. The wedge-like southeasterly wind structure maintains its form through 1200 LST (Figure 16a), with no BL convergence zone developing. Correspondingly, there was no rainfall over north central HNI throughout the daytime. However, rainfall continues to develop over southern HNI, consistent with CTRL (see Figures 4d and 4e), which, according to Wang et al. (2022), is produced by the lifting of enhanced onshore flows related to BL inertial oscillations over the ICP. Due to the absence of daytime BL vertical mixing, low-level convergence fails to develop near noon. Consequently, CI does not occur in north central HNI.

In addition, we also analyzed the diurnally perturbed winds over HNI and the neighboring seas in FixTSK (not shown), just like Figure 14 or CTRL: there is little difference between them. In FixTSK, without the influence of local land-sea breezes over HNI, the diurnal variations of winds on the island should be modulated mainly by the ageostrophic perturbation winds from the upstream, especially ICP. The resemblance of the diurnal variations of winds in FixTSK to those in CTRL further proves that under strong monsoonal southwesterly winds, the diurnal variations of the low-level winds over HNI are dominated by the advected perturbation winds from the upstream, and the role of the local land-sea breezes is secondary and is not responsible for initiating the convection at north central HNI in the afternoon.

4.3.2. The Role of Terrain in Convection Initiation in NoTER Experiment

As for the role of terrain in producing rainfall over the northern HNI, different authors hold differing views. Zhu et al. (2017) believe that the orography is not a dominant factor in the pre-summer precipitation over HNI, while Liang and Wang (2017) suggest that the thermal and dynamical effects of the mountains jointly cause markedly stronger sea-breeze circulations and frontal updrafts, resulting in frequent and intense summer precipitation on the lee side of HNI. Earlier, we showed that the wedge-shaped southeasterly wind structure is a crucial factor in the initiation of northern island convection, and its establishment is closely linked to the dynamic effect of the southern mountains. Here we ask: What would happen to the north island's rainfall if the southern mountains were absent?

In experiment NoTER, we set the height of orography on the entire HNI to 0 m. In the absence of the mountains, the diurnal variations of low-level winds over HNI and the upstream sea (not shown) remain relatively unchanged, closely resembling those in CTRL (see Figure 14). In Figure 17, we show the evolution of 950 hPa winds in the morning of 20 June, with the wind component parallel to line A-B shaded. The advance of northwesterly on HNI, as well as the retreat of southeasterly, is very similar to those in CTRL (cf. Figures 6 and 17). However, the northwesterly on the northern island does not appear until 1100 LST, and its strength (<2 m s^{-1}) is relatively

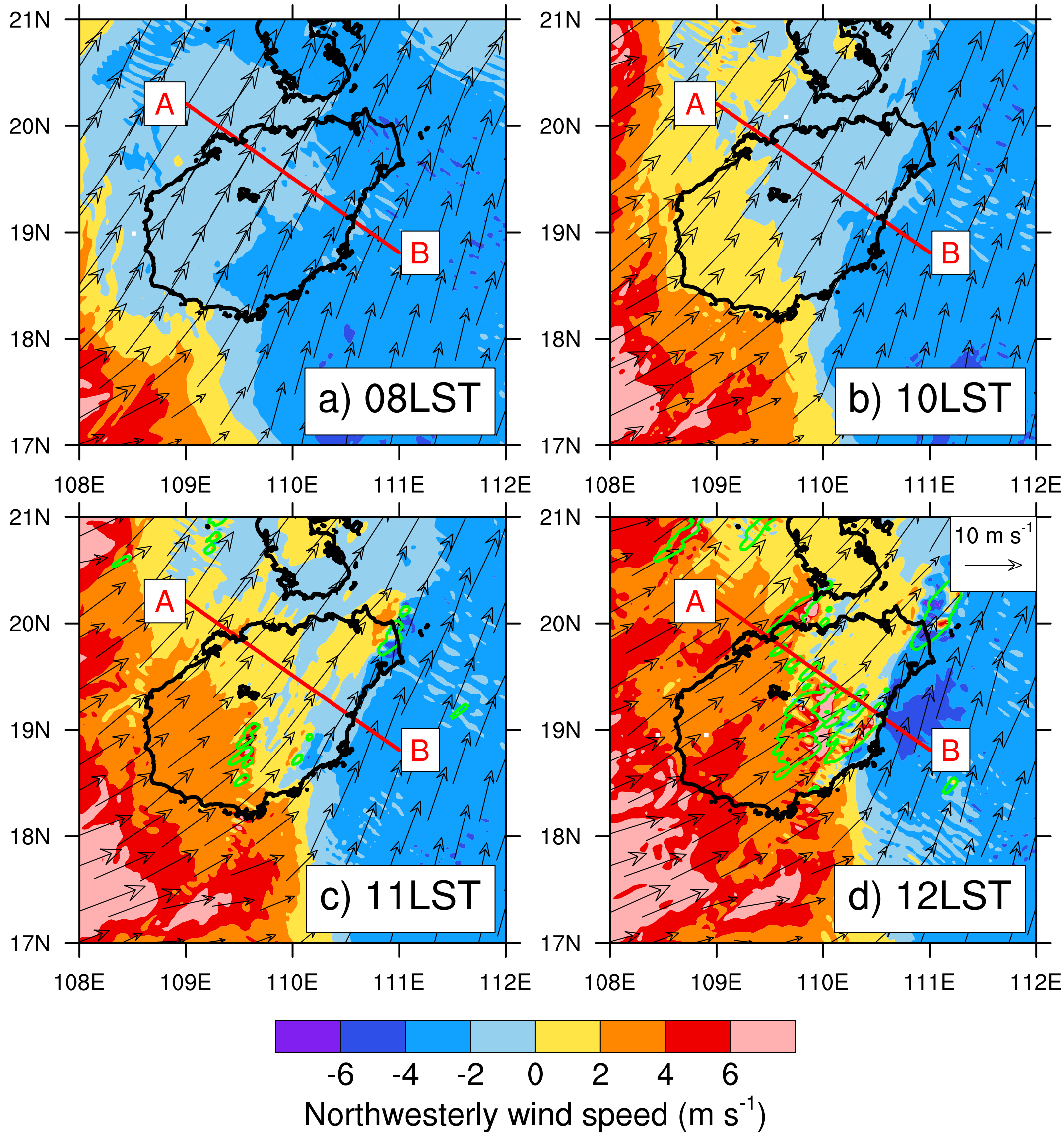

Figure 17. Same as Figure 6, but for the NoTER run. The green solid line represents the contour of 1 mm hr^{-1} rainfall.

weaker compared to 2–4 m s^{-1} in CTRL (cf. Figures 6c and 17c). This is due to the disappearance of nocturnal downslope winds and associated wedge-shaped wind structure in the morning as a result of the absence of the mountain. Without the wedge-shaped wind structure, northwesterly stays higher in the vertical and fails to reach near surface in the morning, leading to a delayed onset and reduced intensity of the 950 hPa northwesterly flow at the north central HNI.

Nonetheless, at 1100 LST (see Figure 17c), a nearly south-north-oriented convergence line forms over the land where northwesterly winds transition to southeasterly, and rainfall begins on the southern island near the line. By 1200 LST (see Figure 17d), rainfall is successively initiated on the northern island, mainly along the convergence line. It shows that rainfall initiation in the north is also tied to the convergence line, similar to the CTRL run, despite the weakened BL vertical mixing (cf. Figures 6d and 17d). Our question is: How does this convergence line form? We notice that it actually evolves from the earlier transitional line between northwesterly and southeasterly, as seen at 0800 LST and 1000 LST (see Figures 17a and 17b). The motion of the line roughly matches the wind speed, indicating that it primarily results from the advection of the perturbed northwesterly winds. This suggests that in the absence of mountain blocking, enhanced horizontal advection partially offsets the weakened effect of BL vertical mixing. Additionally, in the afternoon, rainfall on the island occurs mainly in the north (not shown), a pattern similar to that in CTRL, but the initiation mechanism of such rainfall is very different.

4.3.3. The Role of HCRs

Zhu et al. (2021) suggested that HCRs would interact with sea-breeze fronts and enhance CI on northern HNI under high wind conditions. Since precipitation, once it forms, can interfere with the structure and organization of the HCRs, which we want to focus on, we run experiment NoRAIN with condensational processes turned off, similar to the high-wind DRY experiment in Zhu et al. (2021).

We examined the horizontal divergence on the second model level (about 103 m AGL) to reveal the HCR evolution in NoRAIN and CTRL (Figure 18). At 1000 LST, the divergence fields in NoRAIN and CTRL are nearly identical in northern HNI, and both look a little disorganized (Figures 18a and 18d). By 1200 LST, well-organized northeast-southwest-oriented convergence/divergence strips appear in northern HNI in NoRAIN (Figure 18b) while those in CTRL are affected by rain downdrafts and the rainfall on line A-B is not necessarily located where HCR convergence is the strongest earlier on (Figure 18e). By 1400 LST, multiple strong convergence bands of HCRs become more organized in NoRAIN over northern HNI. There are two convergence bands along the northern coastline and near and inward of the northeastern coastline that are associated with the sea-breeze fronts (Figure 18c). The overall striped pattern resembles that of the high-wind DRY simulations of Zhu et al. (2021) (see their Figures 4b and 4c), although they presented maximum vertical velocity in the lowest 2 km layer instead. Such bands are characteristic of HCRs because their orientations match the BL wind direction (Weckwerth et al., 1999). Furthermore, visible images captured by MODIS/Terra satellite passing over HNI during 1050–1055 LST on 20 June 2017 did show cloud streets that are indicative of the presence of BL HCRs over the northeastern part of the island (not shown, available from NASA Worldview), although the clouds are not very continuous, suggesting that the HCRs were not very strong.

Similar to Zhu et al. (2021), the HCRs in NoRAIN intersect with sea-breeze fronts near the north and northeast coastlines at 1400 LST (cf. Figure 18c and their Figure 4c). However, the intersection points are located near the coastlines and far from the inland CI locations. Therefore, the interaction of HCRs with sea-breeze fronts cannot explain the inland CI occurring as early as 1200 LST in our case (see Figure 18e). Still, do HCRs play any role in the inland CI in the presence of BL vertical mixing-induced convergence zone?

In Figure 19, we present vertical cross-sections of vertical velocity and total liquid–ice condensate along line A-B in NoRAIN and CTRL, together with equivalent potential temperature θ_e contours. At 1100 LST (see Figures 19a and 19c), the BL exhibits organized vertical velocity columns in both experiments, indicative of the HCRs. In particular, aided by the ascending branches of HCRs superimposed on the broader ascent forced by the BL vertical mixing-induced convergence zone (as indicated by the upward bulge of θ_e contours, cf. Figure 10 of Xue and Martin (2006a)), initial clouds emerge in CTRL between 109.6°E and 110°E in the broader convergence zone but at the preferred locations of HCR updrafts (Figure 19c). By 1200 LST, the earlier shallow clouds had developed into deep convection reaching 5 km in height, leading to CIs in that region (Figure 19d). Previous researchers have documented some cases of DMC initiated at the intersection of HCRs with sea-breeze fronts or drylines (Atkins et al., 1995, 1998; Xue & Martin, 2006b). In our case, it is the convergence zone developing out of the downward transport of westerly momentum near the center of northern HNI that plays the role of a sea-breeze front or dryline while the overlaid HCR updrafts trigger the very first clouds and deep convection. The formation mechanism of low-level convergence in our case is very similar to that of dryline convergence (Xue & Martin, 2006b). With the persistent lifting by the convergence zone, CI will eventually occur even without HCRs, albeit with a somewhat delayed timing.

5. Summary and Conclusions

Among the coastal areas of South China prone to extreme rainfall during the East Asian summer monsoon season (mid-May to August), northern Hainan Island (HNI) stands out as a major hotspot for convection and heavy precipitation, especially in the afternoon. Sea-breeze fronts are generally believed to be the primary cause of afternoon rainfall in northern HNI during this period while some studies also pointed to the contribution of BL horizontal convective roll circulations. Based on numerical simulations of a typical case with strong monsoon flows, in which convective initiation (CI) occurred near noon time in north central HNI, this study investigates the primary triggering mechanism for convection. It is found that the convection in the north central HNI is initiated

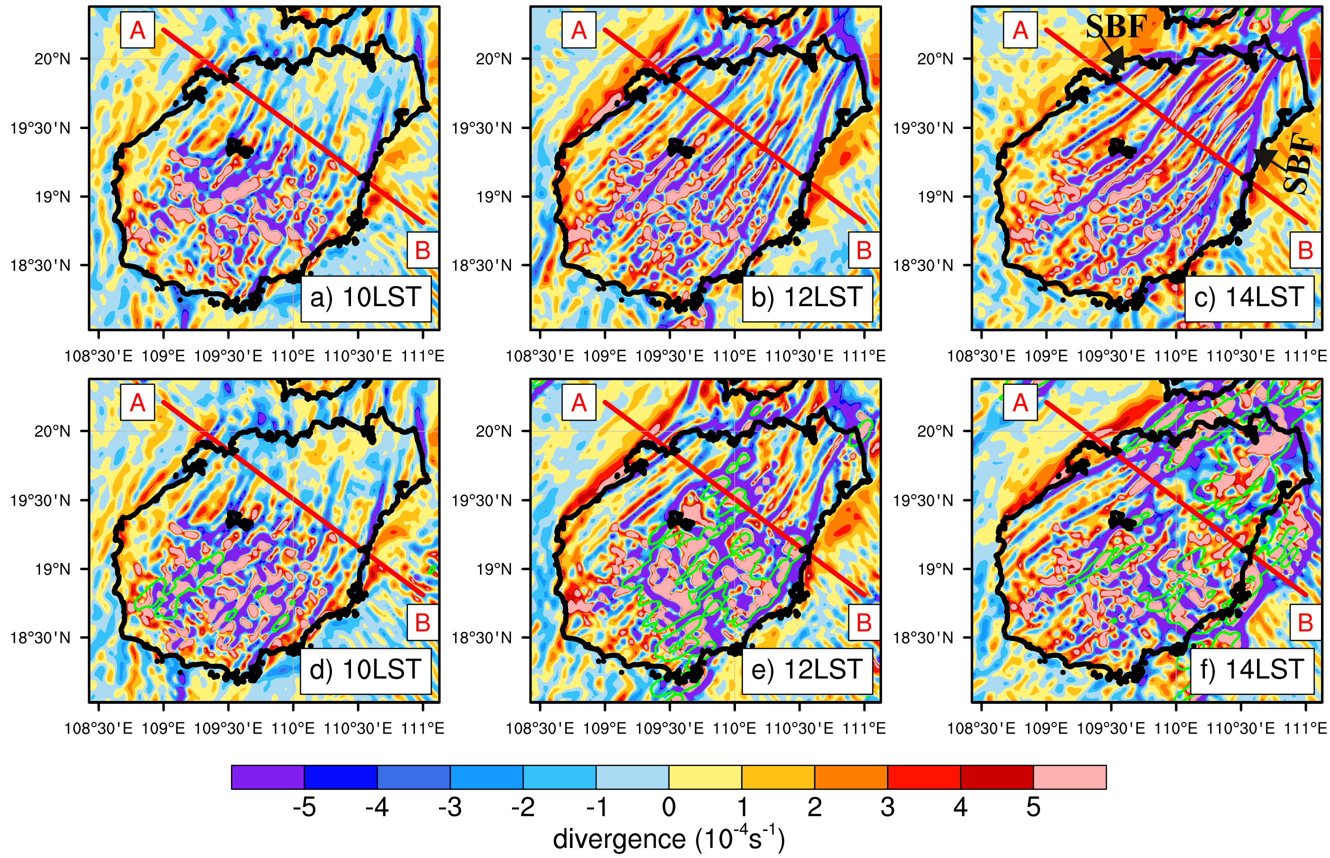

Figure 18. Horizontal wind divergence (shaded) at about 103 m AGL and hourly rainfall over 1 mm hr^{-1} (green solid contours) simulated in NoRAIN (upper panels) and CTRL (lower panels) for 1000 LST (left column), 1200 LST (middle column), and 1400 LST (right column), 20 June 2017. Line A-B is the same as in the previous figures. The labels "SBF" and arrows in (c) indicate the locations of the sea-breeze fronts.

by a convergence zone created by differential downward transport of above-BL westerly momentum by daytime BL vertical mixing while BL horizontal convective rolls (HCRs) play only secondary roles.

The main findings are listed as follows:

1. Under high-wind conditions with strong background southwesterly monsoon flows, a wedge-shaped wind structure forms in the lee of the southern HNI mountains from late night into early morning. This occurs when low-level winds on the windward side of the mountains that have been significantly enhanced by upstream BL inertial oscillations climb over the southern mountains in the morning and descend along the leeside slope. Other flows that circumvent the mountains from the west side enhance the westerly wind component on the lee side. As a result, a layer of flows with a northwesterly wind component overlaying a layer with a southeasterly wind component forms on the lee side, with the depth of the latter decreasing from east toward the west, and such a wedge structure is most evident within a southeast-northwest vertical cross-section.
2. By around noon, BL vertical mixing transports the northwesterly wind component from the upper BL and further up downward toward the surface in the western part, eroding the shallower near-surface southeasterly wind component while the deeper southeasterly wind component remains at the surface to the east. The southeasterly is also reinforced somewhat by an upstream perturbed flow and the sea breeze from the east coast. The contrast between the northwesterly and southeasterly wind components establishes a strong convergence zone in north central HNI. Consequently, CI preferentially occurs within this convergence zone, with the exact timing and locations of initial CIs modulated by the circulations of HCRs in the BL.
3. Under high-wind conditions, diurnal low-level wind variations over the northern HNI are more due to perturbed winds coming from the ICP upstream. While local sea breezes do form along the island downstream flanks, at the northeastern and north/northwest coastlines, their inland penetrations tend to be prevented or retarded by the strong background winds, making it difficult for them to reach the north central HNI and trigger

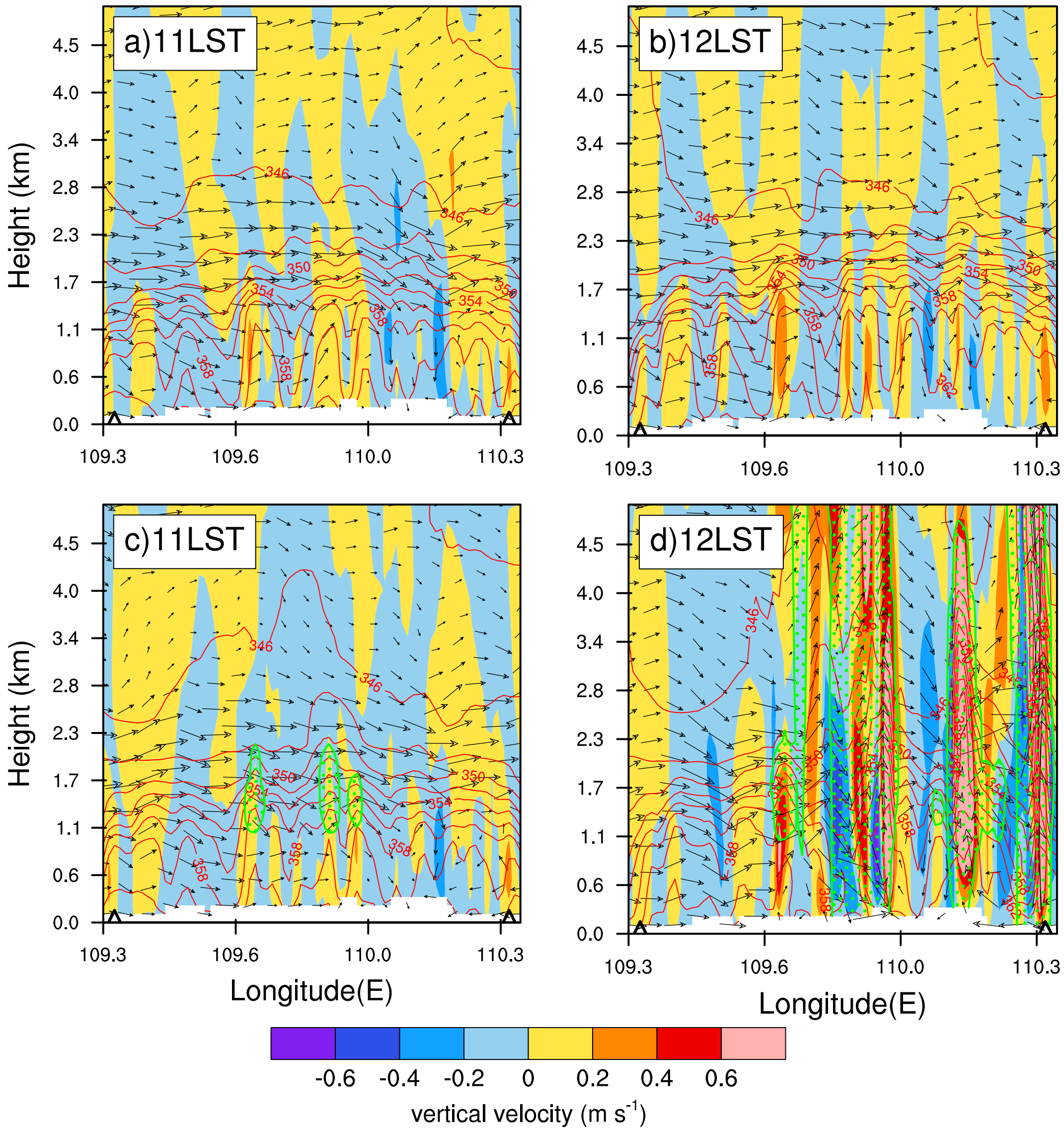

Figure 19. Vertical cross-sections along part of line A-B (see Figure 18) for equivalent potential temperature (red solid, contour interval = 2K), vertical velocity (shaded), 0.01 g kg^{-1} total water-ice condensate outlining the clouds (green solid and stippled), and wind vectors with vertical component amplified by a factor of 10 in NoRAIN (upper panels) and CTRL (lower panels) for 1100 LST (left column) and 1200 LST (right column) 20 June. The triangles on the abscissas mark the west and east coastlines of HNI.

convection there. The direct effect of the southern mountains on CI in north central HNI, in terms of directly creating the low-level convergence that triggers convection, is also limited, despite their roles in shaping the wedge-shaped wind structure.

Based on the above findings, we propose a conceptual model illustrated in Figure 20. At ~0800 LST (Figure 20a), the BL over northern HNI exhibits strong vertical wind shear. It features intrusion of a southeasterly wind component beneath a northwesterly wind component aloft, with the total flows directed northeastwards. A wedge-shaped structure of the southeasterly wind component exists in the BL in response to nocturnal and early morning downslope winds on the lee side of the southern HNI mountains. By ~1000 LST (Figure 20b), daytime BL vertical mixing erodes the shallower southeasterly wind component on the westside in the southeast-northwest cross section, replacing it with downward transported northwesterly winds that oppose the southeasterly on the eastside, creating a convergence zone between them. The forced ascent lifts air parcels in the convergence zone. With time, more of the shallower southeasterly wind wedge gets eroded on the west side, causing an

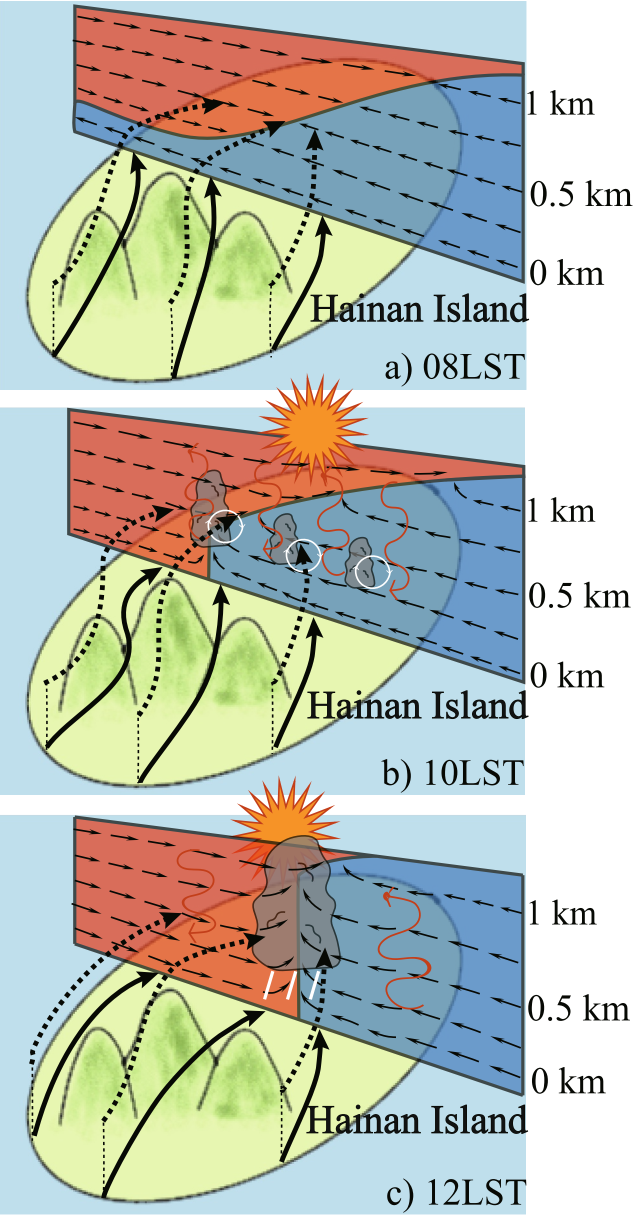

Figure 20. A conceptual model for CI and afternoon rainfall over north central HNI on days with strong monsoon flows. (a) In the early morning, the BL over northern HNI exhibits strong vertical wind shear, with a wedge-shaped southeasterly flow in the lower levels undercutting the northwesterly flow aloft; this wedge pattern results from nocturnal downslope winds on the lee side of the southern NHI mountains. (b) By ~1000 LST, daytime BL vertical mixing erodes the shallower near-surface southeasterly in the west, allowing the upper-level northwesterly to reach the surface; this creates a convergence zone between the northwesterly and southeasterly flows, whose associated ascent lifts air parcels; HCRs and their associated clouds develop in the BL, with those in the convergence zone producing the strongest ascent. (c) By ~1200 LST, the convergence zone has shifted further eastwards due to further erosion of BL vertical mixing, with the associated ascent now significantly stronger; this culminates in the initiation of deep convection in the convergence zone, initially at the locations of HCR clouds. The red (blue) shading denotes the northwesterly (southeasterly) wind component projected onto the vertical cross-section shown. The solid (dotted) black curved arrows indicate air flows on the ground (950 hPa). The gray-shaped regions and white circles in panel (b) mark the HCR clouds and circulations. The red upward or downward curved arrows in panels (b, c) represent the effect of BL vertical mixing.

apparent eastward shift of the surface convergence zone. By ~1200 LST (Figure 20c), the northwesterly dominates the western island while the southeasterly prevails in the east, sharpening the convergence and the associated ascent. Meanwhile, HCRs that have developed within the daytime BL produce localized drafts that are overlaid on the ascent induced in the convergence zone, and convection is first initiated at the locations of HCR updrafts.

The above mechanism bears a strong resemblance to CIs at a dryline in the Great Plains of the United States. In the case of dryline, a wedge-shaped BL with an easterly wind component exists due to underlying sloping terrain, while enhanced BL vertical mixing over the elevated terrain on the west side of dryline brings westerly momentum toward the surface, creating strong surface convergence at the dryline location. The exact timing and locations of initial CIs can be modulated by BL HCRs, whose circulations are superimposed on top of the broader circulation in the convergence zone (Xue & Martin, 2006b). Finally, while we believe that the CI mechanisms revealed in this study for afternoon rainfall in north central HNI are representative of the days with strong background monsoon flows, more cases should be investigated to see if they are indeed generally applicable.

Conflict of Interest

The authors declare no conflicts of interest relevant to this study.

Availability Statement

Hourly precipitation observation data are available from the National Meteorological Information Center of China Meteorological Administration (National Meteorological Information, 2011). NCEP GDAS/FNL analysis data are available from the Geoscience Data Exchange (National Centers for Environmental Prediction, 2015). ERA5 monthly reanalysis data are available from the Copernicus Climate Data Store (Hersbach et al., 2023).

Acknowledgments
This work was primarily supported by the Natural Science Foundation of China (NSFC) Grants 42475161 and 41730965.

References

Atkins, N. T., Wakimoto, R. M., & Weckwerth, T. M. (1995). Observations of the sea-breeze front during CaPE. Part II: Dual-Doppler and aircraft analysis. *Monthly Weather Review*, *123*(4), 944–969. https://doi.org/10.1175/1520-0493(1995)123<0944:ootsbf>2.0.co;2

Atkins, N. T., Wakimoto, R. M., & Ziegler, C. L. (1998). Observations of the finescale structure of a dryline during VORTEX 95. *Monthly Weather Review*, *126*(3), 525–550. https://doi.org/10.1175/1520-0493(1998)126<0525:OOTFSO>2.0.CO;2

Bai, L., Chen, G., & Huang, L. (2020). Convection initiation in monsoon coastal areas (South China). *Geophysical Research Letters*, *47*(11), e2020GL087035. https://doi.org/10.1029/2020GL087035

Blackadar, A. K. (1957). Boundary layer wind maxima and their significance for the growth of nocturnal inversions. *Bulletin of the American Meteorological Society*, *38*(5), 283–290. https://doi.org/10.1175/1520-0477-38.5.283

Chen, X., Zhang, F., & Zhao, K. (2016). Diurnal variations of the land–sea breeze and its related precipitation over south China. *Journal of the Atmospheric Sciences*, *73*(12), 4793–4815. https://doi.org/10.1175/jas-d-16-0106.1

Chen, X., Zhao, K., Ming, X., Bowen, Z., Xuanxuan, H., & Weixin, X. (2015). Radar-observed diurnal cycle and propagation of convection over the Pearl River Delta during Mei-Yu season. *Journal of Geophysical Research: Atmospheres*, *120*(24), 12557–12575. https://doi.org/10.1002/2015JD023872

Chen, X., Zhao, K., & Xue, M. (2014). Spatial and temporal characteristics of warm season convection over Pearl River Delta region, China, based on 3 years of operational radar data. *Journal of Geophysical Research: Atmospheres*, *119*(22), 12447–412465. https://doi.org/10.1002/2014JD021965

Crosman, E. T., & Horel, J. D. (2010). Sea and Lake breezes: A review of numerical studies. *Boundary-Layer Meteorology*, *137*(1), 1–29. https://doi.org/10.1007/s10546-010-9517-9

Du, Y., & Chen, G. (2019). Climatology of low-level jets and their impact on rainfall over Southern China during the early-summer rainy season. *Journal of Climate*, *32*(24), 8813–8833. https://doi.org/10.1175/jcli-d-19-0306.1

Du, Y., Chen, G., Han, B., Mai, C., Bai, L., & Li, M. (2020). Convection initiation and growth at the Coast of South China. Part I: Effect of the marine boundary layer jet. *Monthly Weather Review*, *148*(9), 3847–3869. https://doi.org/10.1175/mwr-d-20-0089.1

Du, Y., Shen, Y., & Chen, G. (2022). Influence of coastal marine boundary layer jets on rainfall in south China. *Advances in Atmospheric Sciences*, *39*(5), 782–801. https://doi.org/10.1007/s00376-021-1195-7

Durran, D. R. (1986). Another look at downslope windstorms. Part I: The development of analogs to supercritical flow in an infinitely deep, continuously stratified fluid. *Journal of the Atmospheric Sciences*, *43*(21), 2527–2543. https://doi.org/10.1175/1520-0469(1986)043<2527:aladwp>2.0.co;2

Hersbach, H., Bell, B., Berrisford, P., Biavati, G., Horányi, A., Muñoz Sabater, J., et al. (2023). ERA5 monthly averaged data on pressure levels from 1940 to present [Dataset]. https://doi.org/10.24381/cds.6860a573

Hong, S.-Y., Noh, Y., & Dudhia, J. (2006). A new vertical diffusion package with an explicit treatment of entrainment processes. *Monthly Weather Review*, *134*(9), 2318–2341. https://doi.org/10.1175/mwr3199.1

Iacono, M. J., Delamere, J. S., Mlawer, E. J., Shephard, M. W., Clough, S. A., & Collins, W. D. (2008). Radiative forcing by long-lived greenhouse gases: Calculations with the AER radiative transfer models. *Journal of Geophysical Research*, *113*(D13). https://doi.org/10.1029/2008jd009944

Jiménez, P. A., Dudhia, J., González-Rouco, J. F., Navarro, J., Montávez, J. P., & García-Bustamante, E. (2012). A revised scheme for the WRF surface layer formulation. *Monthly Weather Review*, *140*(3), 898–918. https://doi.org/10.1175/mwr-d-11-00056.1

Joyce, R. J., Janowiak, J. E., Arkin, P. A., & Xie, P. (2004). CMORPH: A method that produces global precipitation estimates from passive microwave and infrared data at high spatial and temporal resolution. *Journal of Hydrometeorology*, *5*(3), 487–503. https://doi.org/10.1175/1525-7541(2004)005<0487:camtpg>2.0.co;2

Li, J., Li, N., & Yu, R. (2019). Regional differences in hourly precipitation characteristics along the Western Coast of south China. *Journal of Applied Meteorology and Climatology*, *58*(12), 2717–2732. https://doi.org/10.1175/jamc-d-19-0150.1

Liang, Z., & Li, L. (2024). What primarily regulates the evolution of convection in Hainan Island? *Atmospheric Research*, *303*, 107319. https://doi.org/10.1016/j.atmosres.2024.107319

Liang, Z., & Wang, D. (2017). Sea breeze and precipitation over Hainan Island. *Quarterly Journal of the Royal Meteorological Society*, *143*(702), 137–151. https://doi.org/10.1002/qj.2952

Liu, X., Luo, Y., Guan, Z., & Zhang, D.-L. (2018). An extreme rainfall event in coastal south China during SCMREX-2014: Formation and roles of rainband and echo trainings. *Journal of Geophysical Research: Atmospheres*, *123*(17), 9256–9278. https://doi.org/10.1029/2018JD028418

Livneh, B., Restrepo, P. J., & Lettenmaier, D. P. (2011). Development of a unified land model for prediction of surface hydrology and land–atmosphere interactions. *Journal of Hydrometeorology*, *12*(6), 1299–1320. https://doi.org/10.1175/2011jhm1361.1

National Centers for Environmental Prediction. (2015). NCEP GDAS/FNL 0.25 degree global tropospheric analyses and forecast grids [Dataset]. https://doi.org/10.5065/D65Q4T4Z

National Meteorological Information. (2011). China automatic weather station and CMORPH merged hourly precipitation grid dataset V1.0 [Dataset]. Retrieved from https://data.cma.cn/site/subjectDetail/id/101.html

Shen, Y., Zhao, P., Pan, Y., & Yu, J. (2014). A high spatiotemporal gauge-satellite merged precipitation analysis over China. *Journal of Geophysical Research: Atmospheres*, *119*(6), 3063–3075. https://doi.org/10.1002/2013JD020686

Skamarock, W. C., Klemp, J. B., Dudhia, J., Gill, D. O., Barker, D., Duda, M. G., & Powers, J. G. (2008). *A description of the advanced research WRF version 3 (no. NCAR/TN-475+STR)*. University Corporation for Atmospheric Research. https://doi.org/10.5065/D68S4MVH

Thompson, G., Field, P. R., Rasmussen, R. M., & Hall, W. D. (2008). Explicit forecasts of winter precipitation using an improved bulk microphysics scheme. Part II: Implementation of a new snow parameterization. *Monthly Weather Review*, *136*(12), 5095–5115. https://doi.org/10.1175/2008mwr2387.1

Wang, H., Luo, Y., & Jou, B. (2014). Initiation, maintenance, and properties of convection in an extreme rainfall event during SCMREX: Observational analysis. *Journal of Geophysical Research: Atmospheres*, *119*(23). https://doi.org/10.1002/2014JD022339

Wang, X., Xue, M., Zhu, K., Zhang, Y., & Fan, Z. (2022). Diurnal variation of summer monsoon season precipitation over Southern Hainan Island, China: The role of boundary layer inertial oscillations over Indochina Peninsula. *Journal of Geophysical Research: Atmospheres*, *127*(23), e2022JD037114. https://doi.org/10.1029/2022JD037114

Weckwerth, T. M., Horst, T. W., & Wilson, J. W. (1999). An observational study of the evolution of horizontal convective rolls. *Monthly Weather Review*, *127*(9), 2160–2179. https://doi.org/10.1175/1520-0493(1999)127<2160:AOSOTE>2.0.CO;2

Xue, M., & Martin, W. J. (2006a). A high-resolution modeling study of the 24 May 2002 dryline case during IHOP. Part I: Numerical simulation and general evolution of the dryline and convection. *Monthly Weather Review*, *134*(1), 149–171. https://doi.org/10.1175/mwr3071.1

Xue, M., & Martin, W. J. (2006b). A high-resolution modeling study of the 24 May 2002 dryline case during IHOP. Part II: Horizontal convective rolls and convective initiation. *Monthly Weather Review*, *134*(1), 172–191. https://doi.org/10.1175/mwr3072.1

Zhang, Q., Ni, X., & Zhang, F. (2017). Decreasing trend in severe weather occurrence over China during the past 50 years. *Scientific Reports*, *7*(1), 42310. https://doi.org/10.1038/srep42310

Zheng, Y., Xue, M., Li, B., Chen, J., & Tao, Z. (2016). Spatial characteristics of extreme rainfall over China with hourly through 24-hour accumulation periods based on national-level hourly rain gauge data. *Advances in Atmospheric Sciences*, *33*(11), 1218–1232. https://doi.org/10.1007/s00376-016-6128-5

Zhu, L., Bai, L., Chen, G., Sun, Y., & Meng, Z. (2021). Convection initiation associated with ambient winds and local circulations over a tropical island in south China. *Geophysical Research Letters*, *48*(16), e2021GL094382. https://doi.org/10.1029/2021GL094382

Zhu, L., Chen, X., & Bai, L. (2020). Relative roles of low-level wind speed and moisture in the diurnal cycle of rainfall over a tropical island under monsoonal flows. *Geophysical Research Letters*, *47*(8), e2020GL087467. https://doi.org/10.1029/2020gl087467

Zhu, L., Meng, Z., Zhang, F., & Markowski, P. M. (2017). The influence of sea- and land-breeze circulations on the diurnal variability in precipitation over a tropical island. *Atmospheric Chemistry and Physics*, *17*(21), 13213–13232. https://doi.org/10.5194/acp-17-13213-2017